**Ocean Science**

# A vertical-mode decomposition to investigate low-frequency internal motion across the Atlantic at 26° N

**Z. B. Szuts[1], J. R. Blundell[2], M. P. Chidichimo[1,3,\*], and J. Marotzke[1]**

[1]Max Planck Institute for Meteorology, Hamburg, Germany
[2]National Oceanography Centre Southampton, Southampton, UK
[3]International Max Planck Research School on Earth System Modelling, Hamburg, Germany
[*]now at: Graduate School of Oceanography, University of Rhode Island, Narragansett, Rhode Island, USA

*Correspondence to:* Z. B. Szuts (zoltan.szuts@zmaw.de)

**Abstract.** Hydrographic data from full-depth moorings maintained by the Rapid/MOCHA project and spanning the Atlantic at 26° N are decomposed into vertical modes in order to give a dynamical framework for interpreting the observed fluctuations. Vertical modes at each mooring are fit to pressure perturbations using a Gauss-Markov inversion. Away from boundaries, the vertical structure is almost entirely described by the first baroclinic mode, as confirmed by high correlation between the original signal and reconstructions using only the first baroclinic mode. These first baroclinic motions are also highly coherent with altimetric sea surface height (SSH). Within a Rossby radius (45 km) of the western and eastern boundaries, however, the decomposition contains significant variance at higher modes, and there is a corresponding decrease in the agreement between SSH and either the original signal or the first baroclinic mode reconstruction. Compared to the full transport signal, transport fluctuations described by the first baroclinic mode represent < 25 km of the variance within 10 km of the western boundary, in contrast to 60 km at other locations. This decrease occurs within a Rossby radius of the western boundary. At the eastern boundary, a linear combination of many baroclinic modes is required to explain the observed vertical density profile of the seasonal cycle, a result that is consistent with an oceanic response to wind-forcing being trapped to the eastern boundary.

## 1 Introduction

With increased sampling of the oceans over the past decades, the importance and ubiquitousness of low frequency and large-scale waves has become increasingly clear and central to the understanding of ocean dynamics. Although sufficient coverage for interpreting the large spatial scales and long periods of these waves has come from satellite altimetry (Chelton et al., 1998), long duration in situ measurements have not been available to consider the sub-surface signals. An array of full-depth moorings across the Atlantic maintained by the Rapid/MOCHA project since 2004 provide a first description of the internal signature of such motions. Large-scale waves transmit information and energy through the ocean in response to changing forcing or to instability. Theories of the setup and response of ocean gyres to wind-stress or buoyancy input rely on energy being transmitted through the ocean by planetary Rossby waves, or along the ocean margin by boundary waves (Johnson and Marshall, 2002). For the waves to permanently adjust the ocean, however, their energy has to be converted out of the wave motion and into steady motion or altered stratification.

The Rapid/MOCHA array is designed to measure density profiles at the boundary as a means to calculate the geostrophic basin-wide transport, which is a major component of the meridional overturning circulation (Cunningham et al., 2007). To date, density perturbations from waves or eddies have been treated as transient features that are "noise" on top of the low-frequency density signal. A strong reduction of surface eddy motions directly at the western boundary
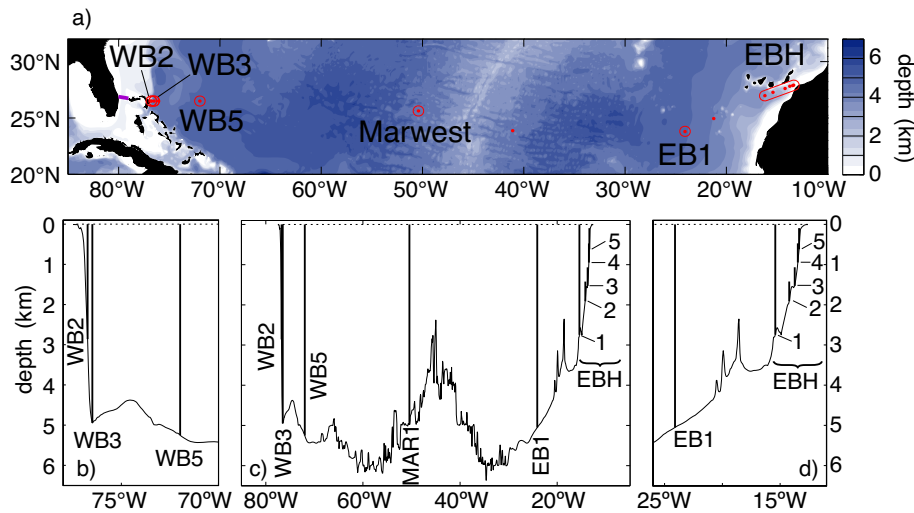
**Fig. 1.** Mooring locations. **(a)** Chart of the Atlantic showing all Rapid/MOCHA moorings (red dots), the 6 moorings used here (circled), and the Florida Current cable (purple line). Cross-section of the transect for the **(b)** western boundary, **(c)** full transect, and **(d)** eastern boundary. The eastern boundary slope moorings (EBH1–EBH5) are shown for the deployment in 2004. Bathymetry comes from ETOPO5.

(Kanzow et al., 2009) obviated concerns that the overturning calculation was swamped by eddy signals (Wunsch, 2008). Viewed in the context of waves transmitting energy around the ocean, however, characterizing the nature of wave signals across the basin is a necessary and initial step towards understanding planetary wave pathways.

The Rapid/MOCHA array collects a dataset unique in vertical resolution and duration (Cunningham et al., 2007) that lets us test hypotheses developed theoretically and numerically with what we observe in the real ocean. Compared to moorings used in a previous study (Wunsch, 1997), the Rapid/MOCHA data have 3–5 times higher vertical resolution and resolve periods 2–4 times longer than typical for moored observations. Our analysis focuses on perturbations that span the water column and that can be consistently extracted from 5.5 years of observations. The fortuitous placement of these moorings spanning a subtropical basin gives insight into the pathways of planetary waves on a basin scale. Characterizing the wave signals across the basin will suggest the forcing regions, mechanisms, and energy transport of such features.

Here we develop a technique to fit vertical modes to the hydrographic measurements and illustrate how it allows interpretation of the data. The use of theoretically derived vertical modes provides a dynamical framework for interpretation. Further, given the goal of the array to measure the Atlantic meridional overturning circulation, the influence of full water-column signals to this large-scale transport is investigated.

The article sequentially treats the following topics: data sources (Sect. 2); theory of vertical modes (Sect. 3); numerics of the decomposition (Sect. 4); an evaluation of the signal reconstructed from the decomposition and its consistency

with altimetric sea surface height (SSH) (Sect. 5); interpretation and implications of our results (Sect. 6); and a brief conclusion (Sect. 7).

## 2   Data

Moorings have been maintained since February 2004 across the North Atlantic at 26.5° N as part of the Rapid/MOCHA project. The moorings are designed to measure dynamic height, and as such are equipped with moored CTDs (Seabird microcats) in the water column. Though there are also bottom pressure measurements at all moorings and direct velocity measurements at the western boundary (Kanzow et al., 2008), we only present results from the moored CTDs.

### 2.1   Mooring observations

We consider the five full-depth moorings and the eastern boundary mooring (Fig. 1), which are called from west to east, WB2, WB3, WB5, MarWest, EB1, and EBH. The western boundary moorings (WB2, WB3, and WB5) are locate, 15, 40, and 490 km east of the Bahama continental shelf, respectively; MarWest is on the western flank of the Mid-Atlantic Ridge; EB1 is 1200 km west of the North African coast, and EBH is a synthetic profile of multiple moorings along the African continental slope that are 20–120 km from the coast. WB2 is located in water 4000 m deep along the base of the continental slope. EB1 is in water 5000 m deep at the very bottom of the African continental shelf. The EBH synthetic profile is created by vertically concatenating the series of short moorings on the African continental slope. Though EBH is not a single vertical profile and so cannot strictly be interpreted with a vertical mode analysis, we

include it in our analysis to see how well its variability can be explained by these simple assumptions. To focus on the near-boundary region, we terminate the EBH synthetic mooring at EBH1, yielding a profile down to 3000 m. More detailed discussion of this point is given in the Discussion, but for now we note that our approach is consistent with Kanzow et al. (2010).

There are important differences between our analysis and that used to calculate mid-ocean and overturning transports by Cunningham et al. (2007) and others. They calculate mid-ocean or interior geostrophic transport between WB2 and EBH, but both profiles are extended to 5000 m by using data from deeper instruments on moorings further offshore. In addition, direct velocity measurements inshore of WB2 are used to capture energetic surface currents and transports east of the Bahamas in what is called the western boundary wedge. For calculating the overturning circulation, the density profiles are only interpolated to the depth of the shallowest microcat. The interpolation to the surface is derived by mass conservation: when all profiles of transport per unit depth are added together (from geostrophic interior transport, Ekman transport, Florida Current transport, and western boundary wedge transport), the profile must go to zero at the surface and the bottom to conserve mass (Kanzow et al., 2007).

The moored microcats are deployed for one year before mooring turnover, and the bottom pressure sensors are deployed for two years but with two sensors overlapping for one year at each location. Records have week-long gaps between retrieval and recovery. Each mooring has 12–24 microcats in the vertical, with a separation of 50–100 m near the surface increasing to a separation of 500 m below 2000 m. Time series of median sensor depths are shown later in Fig. 4a.

The specific deployment strategy and geometry has evolved since 2004, so each year's mooring geometry is not necessarily identical to that for other years. Sensor failures and full or partial mooring failures introduce temporal gaps that also contribute to differences between deployments. The MarWest mooring site was relocated to a location that was 400 m deeper after the first two years (from a depth of 4815 m to 5215 m). Otherwise, all deployments at the other mooring sites maintained a consistent water depth.

The microcats are calibrated before deployment and after recovery by deploying them together with a highly accurate ship-lowered CTD and adjusting them to agree with the CTD. This calibration procedure makes the microcats accurate to 0.001 °C for temperature, 0.002 psu for salinity, and 5–10 db for pressure. The bottom pressure recorders (BPRs), although they are accurate to 0.001 db, suffer from exponential drift when first subjected to the high pressure at the bottom of the ocean. These pressure drifts are fit with an exponential plus linear drift (Watts and Kontoyiannis, 1990; Kanzow et al., 2007). This behavior means that the absolute value of the bottom pressure is not suitable for analysis, and that

BPR measurements at a significant fraction of the deployment period ($>$ 6 months for a 2 year deployment) may be contaminated by the drift removal. As part of standard data processing procedures (Kanzow et al., 2010), tides and other high frequency signals are removed from each instrumental record with a 2-day low-pass Butterworth filter.

## 2.2 Processing moored hydrographic data

To prepare the data for mode-fitting, we need to remove the effect of mooring motion and calculate a wave perturbation quantity. The procedure used by Rapid/MOCHA to generate profiles of temperature and salinity effectively removes mooring motion. This point is discussed in detail because of its importance to calculating wave perturbations.

Mooring motion is used to describe how horizontal water motion pushes moorings over and downward. When hydrographic data is collected from an instrument that does not remain at a constant depth level, the measured signal will include a signal related to the stratification, in addition to the signal of interest caused by time-evolving ocean flow. We need to take care that mooring motion does not bias our estimates of wave perturbations. A common method when considering a database of moored measurements is to remove moorings that exhibit significant correlation between temperature and pressure (Alford, 2003), but this approach is not an option when considering specific moorings. For instance, mooring WB3 can be knocked down several hundred meters because it is located near the center of the Deep Western Boundary Current, and even in quieter locations such as at EB1 vertical motion is typically 50–100 m in amplitude.

To depth-level the moorings and remove the influence of mooring motion, we use the same vertical interpolation technique used by the Rapid/MOCHA project (Cunningham et al., 2007). This procedure grids microcat measurements of temperature and salinity onto a 20-db grid using climatological gradients of temperature and salinity to interpolate between instruments (for details see Johns et al., 2005). A single temperature measurement $T_1$ at a known pressure $p_1$ is integrated downward to the next sensor ($T_2$, $p_2$) using climatological gradients $\mathrm{d}\overline{T}/\mathrm{d}p$. Because in general the measured $T_1$ is not at the same depth as in the climatology $\overline{T}(p)$, the integral starts at $p_1$ using $\mathrm{d}\overline{T}/\mathrm{d}p$ initiated at the climatological depth of $T_1$. When integrated down to $p_2$, this downward integral will in general give a different temperature than the measured $T_2$. The same procedure is used to integrate upward from sensor 2. The next step is to create a smooth profile that goes through both measurements. Between sensors 1 and 2, the upward and downward integrals are added together with linear weights that go from 0 to 1, such that the measured values are preserved at the sensor depths. For instance, halfway between the sensors the interpolated value is the average of the upward and downward integrations.

This interpolation technique is used in two ways. The first way is to generate a continuous profile from the deepest to

the shallowest instrument, exactly the same as done for regular Rapid/MOCHA processing. The second way is for calculating wave perturbations for each sensor. Instead of interpolating onto a regular grid, each sensor is gridded to its median sensor depth over its deployment. This is depth-leveling, in that it removes the influence of climatological stratification over a short vertical distance in order to calculate wave perturbations.

This approach to depth-leveling microcat records can be quantified by comparing correlations between pressure and temperature before and after the leveling. If there is significant mooring motion, then pressure and temperature will be negatively correlated. Regardless of mooring, the depth-leveling acts to make such correlations more positive. At WB3 the correction is critical because of large knock-down by strong horizontal currents, changing the correlations from a median value of $r = -0.65$ before leveling to $-0.08$ after. The leveling is also significant for moorings with weak buoyancy (e.g. the first and second deployments of WB2), which also experience stronger than normal mooring motion. At other moorings the increase in $r$ is 0.05–0.10, which is typically larger for instruments shallower than 1000 m, and does not alter the generally weak correlations between pressure and either temperature or salinity.

The continuously gridded temperature and salinity profiles are then used to calculate density, which is integrated vertically to yield reduced pressure following MacKinnon and Gregg (2003); Lee et al. (2006):

$$p_r = \frac{g}{\rho_0} \int_z^0 \rho(z)\,\mathrm{d}z + C. \tag{1}$$

Reduced pressure is dynamically equivalent to geopotential anomaly (Appendix A) and so requires a choice of reference level as indicated by $C$. That $p_r$ is based on a vertical integral downward from the surface is problematic because the shallowest instrument is not at the surface and its depth (typically between 50 and 120 m) changes with deployment. Accordingly, we choose the deepest measurement depth on each mooring to be the reference level.

To reflect that there are only a limited number of sensors on each mooring, we only use one measurement per sensor instead of a continuous profile. Each sensor's median depth is used to extract $p_r$, and then the time-average is subtracted to obtain the pressure perturbation $p_r'$. This quantity is depth-leveled.

The near-surface layer is problematic because it is strongly influenced by the atmosphere, such as by seasonal heating, buoyancy fluxes, or wind-input of kinetic energy. These signals are not expected to be indicative of, or coherent with, the full water column wave signal. We remove the influence of such surface processes on our analysis here by not using any instruments whose median depth is shallower than 140 m for WB2, WB3, and WB5, or shallower than 200 m

for MarWest, EB1, and EBH. In addition to containing large signals from processes not of interest here, near-surface measurements lead to numerical instability in the decomposition, as discussed later.

Gridding and time-averaging can only be done meaningfully over a single deployment period. No sensors are at exactly the same depth for different deployments because of changes in mooring geometry. There are only well-defined time-averages over a single deployment, and, correspondingly, wave-perturbations can only be calculated over the same time interval (1 to 1.5 years). Some deployments of microcats last for a relatively short period of time, especially those at EBH where each depth-level is turned over individually. To be able to maintain a meaningful time-average, only deployments longer than 115 days are included in this analysis.

The approach described above can be summarized by the following steps that take the direct measurements to the quantities used for mode fitting: (1) interpolate the temperature and salinity measurements to a vertical grid using climatological gradients, (2) calculate density profiles, (3) calculate $p_r$ using Eq. (1), (4) subtract $p_r(z_{\mathrm{bottom}})$ from $p_r(z)$ at each time step, (5) interpolate $p_r$ at the median depth of each sensor, and (6) subtract the time-average to obtain $p_r'$.

## 2.3 Satellite altimetry

Sea surface height (SSH) comes from altimetry, and specifically from the reference series of the DT-MADT product from Aviso. This is a product made by optimally interpolating corrected along-track data onto a 1/3° by 1/3° grid every 7 days. Note that, in addition to standard tidal corrections, corrections are also made for static atmospheric loading (inverse barometer effect) as well as for the high-frequency barotropic response of the ocean to changes in atmospheric sea level pressure. These geophysical corrections are applied to the along-track data before optimal interpolation, and so barotropic signals cannot be diagnosed from the gridded SSH product. Although the 10-day repeat period of the Jason-1 and Jason-2 orbits formally gives a Nyquist period of 20 days, large-scale signals will be sampled by adjacent tracks and so periods shorter than the Nyquist frequency may be resolved for signals with large enough spatial scales. The reference series means that only data from a Jason satellite (either Jason-1 or Jason-2) and from Envisat (repeat period of 35 days) are used, which provides a dataset with homogeneous temporal sampling and related errors. SSH is interpolated to the locations of the moorings.

Unlike subsurface moorings, SSH is a surface measurement that responds to multiple near-surface processes. The most obvious surface signal unrelated to full-water column motion is seasonal heating and cooling, which only depends on latitude: this we remove by subtracting the zonal average of SSH across the Atlantic. No effort is made to remove other seasonal cycles that may exist in the data (Ekman transport,

coastal upwelling, seasonality of ocean circulation, etc.), as they are more technically challenging to remove and may overlap with our interest in full-depth baroclinic motion.

## 3 Vertical modes

When considering oscillatory signals in the ocean that fill the water column, the vertical dimension can be separated from the equations of motion to yield discrete vertical shapes of variability. Stratification strongly alters the mode shapes, and a large number of assumptions can be made to arrive at various forms of modes. We proceed with two of the more familiar assumptions: modes in a flat-bottomed and motionless ocean (e.g. Gill, 1982), and modes that include realistic topography and geostrophic circulation derived from a hydrographic climatology (Killworth and Blundell, 2003).

### 3.1 An ocean with flat bathymetry and no background motion

The simplest theoretical assumptions are a flat-bottomed ocean in a motionless background state. With the quasi-geostrophic approximation, two equations result (e.g. Gill, 1982; Wunsch and Stammer, 1997):

$$\rho_0 \frac{\partial^2 w}{\partial z \, \partial t} = \left( \frac{\partial^2}{\partial x^2} + \frac{\partial^2}{\partial y^2} \right) p'$$

$$N^2 w = \frac{1}{\rho_0} \frac{\partial^2 p'}{\partial z \, \partial t}, \tag{2}$$

where $\rho_0(z)$ is a reference density profile, $N^2(z)$ is the buoyancy frequency, and $w$ and $p'$ are perturbation quantities of vertical velocity and pressure perturbation. Horizontal velocities can be calculated from the momentum equations and have a phase relationship to $w$ and $p'$ described by polarization relations.

The two equations in Eq. (2) are separable in $z$ and yield two vertical structures, $F_n(z)$ and $G_n(z)$, for a given mode number $n = 0, 1, \ldots$. $F_n$ describes the vertical shapes of $u, v, p'$, while $G_n$ describes that of $w$ and vertical displacement $\xi$. Different modes are vertically orthogonal to one other, and each is normalized to have unit magnitude when projected onto itself. The orthonormality conditions require no scaling for $F_n$ and scaling by $N^2$ for $G_n$. The boundary conditions are $\mathrm{d}F_n/\mathrm{d}z = 0$ at $z = 0, -H$, and $G_n = 0$ at $z = 0, -H$. These mode shapes will be referred to as flat-bottomed (or FB) modes to distinguish them from the modes defined in the following subsection.

The modes are calculated numerically by solving

$$\frac{\mathrm{d}^2 G_n(z)}{\mathrm{d}z^2} + \frac{N^2(z)}{c_n^2} G_n(z) = 0 \qquad \text{or}$$

$$\frac{\mathrm{d}}{\mathrm{d}z} \left( \frac{1}{N^2(z)} \frac{\mathrm{d}F_n}{\mathrm{d}z} \right) + \frac{1}{c^2} F_n(z) = 0, \tag{3}$$
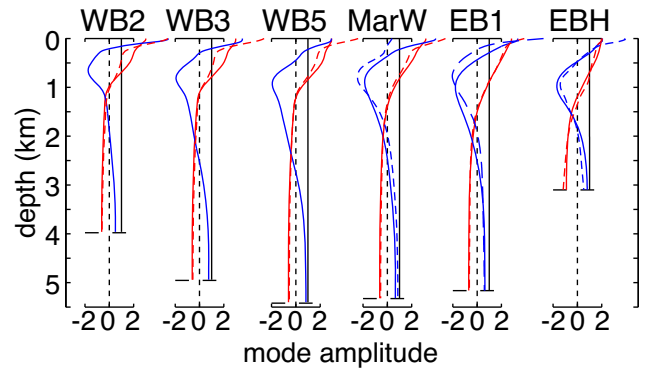


**Fig. 2.** Vertical mode shapes at each station, for depth-uniform modes (black), flat-bottomed baroclinic modes 1 (red solid) and 2 (blue solid), and KB baroclinic modes 1 (dashed red) and 2 (dashed blue, only calculable at stations MarWest, EB1, and EBH). The local water depth is indicated by a dashed horizontal line. The modes are normalized to unit vertical rms and are dimensionless.

where $c_n$ is a separation constant whose physical interpretation is the phase speed for an internal gravity wave with mode $n$. The only input is the stratification profile $N^2(z)$, which is calculated following the method of Chelton et al. (1998) from the climatological $T/S$ profiles used for the gridding procedure.

For this study, we consider reduced pressure perturbation $p'_r = p'/\rho_0$ (in $\mathrm{m}^2 \, \mathrm{s}^{-2}$) which is expanded in terms of modes as

$$p'_r(x, y, z, t) = \sum_{n=0}^{\infty} P_n(x, y, t) \, F_n(z). \tag{4}$$

We adopt the convention of keeping the modal amplitude $P_n$ in physical units such that $F_n$ is dimensionless.

Representative mode shapes are shown for the stratification at each mooring (Fig. 2). The zero-crossing of the first baroclinic mode is close to the base of the thermocline. Heading from the Bahamas eastward across the Atlantic, the depth of the first mode zero-crossing deepens: 970 m at WB2, 1100 m at WB3, 1210 m at WB5, 1360 m at MarWest, 1510 m at EB1, and 1090 m at EBH. Since the location of MarWest was changed after the first two years, two different vertical modes are used to account for the significant change in water depth.

### 3.2 An ocean with sloping bathymetry and mean circulation

A significant body of literature (Killworth et al., 1997; Chelton et al., 1998) found that sloping topography and time-averaged ocean currents alter the propagation speeds noticeably from the flat-bottomed case. We follow the derivation of Killworth and Blundell (2003) and use their algorithms to calculate more realistic modes at the mooring locations in the long-wavelength limit. These results will be referred

to as KB modes. Though they derive the vertical modes $G(z)$ for vertical velocity or isopycnal displacement, it is straightforward to calculate the $F(z)$ modes of interest from $F(z) = dG/dz$ (Wunsch and Stammer, 1997; Killworth and Blundell, 2003). With a Wentzel-Kramers-Brillouin-Jeffreys (WKBJ) approximation in the horizontal, the equations of motion for small perturbations yield a vertical ODE for $G_n(z)$ of the form

$$\frac{d}{dz}\left[\frac{dG_n}{dz}\frac{1}{R}\right] + \frac{S}{R^2}G_n = 0, \tag{5}$$

where $S$ accounts for non-uniform stratification and $R$ is (minus) the locally Doppler-shifted frequency:

$$S = kN^2(z)/f \tag{6}$$
$$R = k\overline{u}(z) + l\overline{v}(z) - \omega. \tag{7}$$

Zonal and meridional wavenumbers are given by $k$ and $l$. Compared to Killworth and Blundell (2003), all equations have been recast into Cartesian coordinates and variables have been renamed for consistency with the flat-bottomed theory presented earlier. The boundary conditions are

$$G = 0 \qquad \text{at } z = 0 \tag{8}$$
$$\frac{dG}{dz} = 1 \qquad \text{at } z = 0 \tag{9}$$
$$G = -\alpha\frac{dG}{dz} \qquad \text{at } z = -H, \tag{10}$$

where $\alpha$ is a parameter that represents the effect of bottom slope

$$\alpha = \left(\frac{\partial H}{\partial y} - \frac{l}{k}\frac{\partial H}{\partial x}\right). \tag{11}$$

The first boundary condition (8) is a rigid lid condition suitable for free waves, while the second (9) is merely for scaling purposes. The third (10) is a kinematic boundary condition of no flow normal to the bottom, which reduces to $\alpha = \partial H/\partial y$ for a purely westward propagating wave with $l = 0$.

The complexity of the formulation is reflected by the facts that KB vertical modes no longer maintain orthogonality, and that higher modes often can not be found because of lack of convergence of the numerical algorithm (Killworth and Blundell, 2003). Generally, the vertical modes at any one location depend on frequency and wavenumber, in addition to the predetermined topographic slopes. The calculated solutions are the long wave-length limit of the general case. In this limit the waves are non-dispersive, and the solutions only depend on the direction of the wavenumber vector $(k, l)$ and not its magnitude. In addition to calculating $G(z)$ and $F(z)$, Killworth and Blundell (2003) also calculate group velocity by expanding the unknown dispersion relation into integrals and terms from Eq. (5) that can be numerically evaluated. Because of the long-wavelength limit, the resulting group velocity is independent of $\omega$ and only depends on the propagation direction.

For the purposes here of comparing KB modes to flat-bottomed modes, we only solve for KB modes that propagate due west with $l = 0$. Solutions are only found at all mooring locations for the first mode, though the second mode is also found at MarWest, EB1, and EBH. The first baroclinic modes from the KB solution (Fig. 2), compared against the flat-bottomed modes, generally have deeper zero-crossings except at WB3 and WB5: 1032 m at WB2, 1080 m at WB3, 1185 m at WB5, 1394 m at MarWest, 1539 m at EB1, and 1225 m at EBH.

## 4   Mode Fitting

Observations used to investigate internal waves, though commonly interpreted in terms of modes, are usually obtained with very different sampling strategies than those used by Rapid/MOCHA. Typically, modes are fit to either moored current meters or repeat hydrographic profiles. The Rapid/MOCHA sampling strategy of moored hydrographic observations requires a combination of existing mode-fitting approaches. In particular, we need to balance a discrete number of sampling depths in the vertical against the use of continuous hydrographic profiles in the literature.

### 4.1   Reduced pressure perturbation

From hydrographic data, there are three quantities that could be used to fit vertical modes to: (1) density perturbations $\rho'$, (2) isopycnal displacements $\xi$, or (3) pressure perturbations $p'$. We choose to work with pressure perturbations and explain below our reasoning.

Density perturbations are as close to the direct measurements as possible. Despite this, they are hardly ever invoked or discussed, with Woodgate and Killworth (1996) being the only recent study the authors could find. Interpreting density modes would be unable to benefit from the broad literature based on $F$ or $G$ modes.

Isopycnal displacements are often used in the literature to investigate internal waves and require the use of vertical modes as given by $G_n(z)$. This variable has the advantage of being calculated from the directly measured density anomaly via

$$\xi = \frac{\rho'(z)}{d\rho_0/dz}. \tag{12}$$

The choice of density gradient $d\rho_0/dz$ relies on the same climatological gradients used for the gridding procedure. There are two difficulties with using isopycnal displacements, one numerical and one interpretational. In terms of numerics, because of the limited degrees of freedom, standard linear regressions are not well constrained and so we need to turn to Gauss-Markov inversion instead. For fitting $G_n(z)$ to isopycnal displacements, however, the residuals need to be weighted by $N^2$ (Gill, 1982). Even though the weighting by $N^2$ can be incorporated into the numerical inversion

done for Gauss-Markov inversion, incorporating the weighting into other aspects of the numerics is not straightforward, in particular assigning a priori uncertainty to the measurements and calculating a posteriori confidence limits. In terms of interpretation, the modes $G_n(z)$ are not as easy to relate to other data sets. First, the barotropic mode is not well defined for $G(z)$, which precludes comparison with bottom pressure records. Second, surface or bottom intensified signals in the observations cannot be efficiently explained by $G_n$ because it vanishes at the surface and seafloor by definition. Third, SSH is often expressed in terms of pressure perturbation at the surface, whereas the relation between SSH and isopycnal displacement contains a frequency-dependent phase lag.

This leaves pressure perturbation $p'$ from Eq. (1) as the quantity that will be considered for the rest of the article, with the corresponding vertical modes $F_n(z)$. Similar relations to Eq. (1) exist for calculating $p'$ by integrating $N^2\xi$ (Kunze et al., 2002), but we prefer to start from $\rho(z)$ because this quantity relies on the climatological profiles only once (in the vertical gridding procedure for $\rho$), instead of 3 times when using $\xi$ (once for $\rho$, once for $\partial\rho/\partial z$, and once for $N^2$ inside the integral).

An additional advantage to the choice of $p'_r$ is its dynamical equivalence to perturbations of geopotential anomaly (Appendix A1). This correspondence allows direct comparison between mode-based reconstructions of reduced pressure perturbation and geostrophic transports. At the same time, difficulties are introduced by requiring a choice to be made for reference level (Appendix A2). We proceed by using the same treatment for the original hydrographic data and the modes wherein a depth-uniform constant is undetermined.

## 4.2 Numerics of mode fitting with discrete inversion

Numerically, there are two ways to fit vertical modes to $p'_r$: using an integral method based on continuous profiles, or using an inverse method on point measurements. We choose the latter for our analysis, because each mooring only has a limited degrees of freedom corresponding to the number of instruments deployed.

Although the integral and inverse methods for mode fitting give very similar results when there are many degrees of freedom and equal vertical spacing, that is not the case for mooring data. The integral method is typically used with CTD profiles that have a very fine and uniform vertical spacing (Lee et al., 2006), whereas an inverse is typically used for current meters that have only a few instruments on each mooring at unequal vertical spacing. The dynamic height moorings have much greater vertical resolution (12–24) than is typical for current meter moorings (usually 3–5 in the database used by Wunsch, 1997). In fact, all of the Rapid/MOCHA moorings meet exacting criteria given by Wunsch (1997), compared with none of the records in his database: being in deep water, having at least 6 instruments, and lasting 2 years or longer in total. Technical reasons prevent a single mooring from being

deployed for longer than 2 years (typically 1–1.5 years for Rapid/MOCHA moorings), but redeployments over multiple years will still capture intermittent but strong signals and provide a good temporal average of periods shorter than the deployment duration. Calculating time-averages over each deployment period will reduce the intensity of signals with periods longer than a year, but such signals would still show up as near-linear trends in each deployment.

The mode fit to $p'_r$ is expressed as

$$\widehat{p_r}'(z,t) = \sum_{n=0}^{M-1} \widehat{P}_n(t)F_n(z) = p'_r(z,t) + \epsilon, \qquad (13)$$

where the notation $\widehat{\cdot}$ indicates the value obtained by inversion, $M$ is the number of modes included in the fit, and $\epsilon$ is random error in measurements or the fit. The barotropic mode is $n = 0$, while the highest baroclinic mode is $M - 1$. The inverse results using flat-bottomed modes are satisfactory at all stations when $M = 5$, where our criteria are explained in detail below and in Sect. 5.2. When using KB modes we use $M = 2$, which is only the depth-uniform mode and the first KB baroclinic mode because only the first KB baroclinic mode can be calculated at all stations.

Algebraically, Eq. (13) can be rewritten as

$$\mathsf{A}\boldsymbol{P} + \boldsymbol{\epsilon} = \boldsymbol{B}_{p'}. \qquad (14)$$

The variable $\mathsf{A}$ (size $J \times M$) is the basis function matrix containing in its $i$th column $F_i(z_j)$; $\boldsymbol{P}$ is a column vector of the $M$ modal amplitudes to be determined; $\boldsymbol{\epsilon}$ is a column vector of error; and $\boldsymbol{B}_{p'}$ is a column vector of the $J$ observations of $p'_r$.

Although these equations can readily be solved with least squares, least squares often gives unrealistically large values for $\widehat{P}_n$. With no constraint other than minimizing the mean residual, least squares regression often finds very large coefficients whose sum cancels at the observation depths, at the expense of having large values between constrained depths. This is especially problematic when the basis functions are hard to distinguish based on the depths of the measurements.

An alternative approach called the Gauss-Markov method (Wunsch, 1996) allows more physical specifications to be included. In contrast to a least-square estimate, the Gauss-Markov estimate minimizes the variance of the fit and thus gives a more stable solution. In practice, the solution has a smooth vertical structure that comes from limiting the magnitude of the fit between data points. In addition, uncertainties of the mode amplitudes can be calculated directly with a priori formulae. The modal amplitudes are found by

$$\widehat{\boldsymbol{P}} = \mathsf{B}_0\mathsf{A}^\mathsf{T}\left(\mathsf{A}\mathsf{B}_0\mathsf{A}^\mathsf{T} + \mathsf{I}_J\sigma^2\right)^{-1}\boldsymbol{B}_{p'}, \qquad (15)$$

where $\mathsf{B}_0$ is an a priori estimate of the variance of the modal amplitudes, $\mathsf{I}_J$ is the identity matrix of size $J$, and $\sigma^2$ is the accuracy of the observations. We start with the assumption

that all modal amplitudes are equal, which is implemented by setting $B_0$ to be a unit matrix multiplied by the average variance of $p'$ at all depths. The uncertainty in the measurements $\sigma^2$ is set to $0.0002 \text{ m}^2\text{ s}^{-2}$, based on the resolution of $p'$. The error covariance matrix is given (Wunsch, 1997) as

$$B_1 = B_0 - B_0 A^T \left( A B_0 A^T + I_J \sigma^2 \right)^{-1} A B_0. \tag{16}$$

The error in each estimate of the modal amplitude $P_n$ is $(B_{1,nn})^{1/2}$.

We purposely choose the number of modes $M$ to be less than the number of instruments $J$. If we had chosen $M = J$ and performed a least squares inversion, then a complete decomposition would result and the signal could be exactly reconstituted from the basis functions. Such an inversion is very unstable, however. The combination of using Gauss-Markov inversion and $M < J$ leads to a smoother result that is hopefully more physically relevant. Despite this choice, we must still verify what mode numbers have unambiguous signals that are not affected by the number and vertical distribution of the measurements.

For comparison with the KB modes for which $M = 2$ is used, it is necessary to perform an additional decomposition with flat-bottomed modes for $M = 2$. This stems from numerical issues related to the orthogonality of the modes when evaluated at the sensor depths. The vertical modes are calculated and made orthogonal on a much finer vertical grid than the measurements, and so orthogonality is not maintained when the modes are evaluated at the depths of the sensors. Vertical gaps caused by sensor failure and by a lack of near-surface measurements contribute to this problem. For lack of perfect orthogonality, modes that partially overlap will share variance between them when many modes are included. As a result, the decomposition with $M = 2$ has more energy in the two modes than does the decomposition with $M = 5$. An equal comparison between the flat-bottomed and KB mode decompositions thus requires $M = 2$ to be used for both.

In comparison to the Gauss-Markov method, an integral method for mode fitting (Gill, 1982; Kunze et al., 2002) based on the continuous gridded profiles would treat errors in a very different manner. Integral methods are often used with continuous CTD/velocity profiles that have data points every meter or two, which is in contrast to the procedure of gridding moored hydrographic measurements using only 12–24 independent samples. If we were to perform a fit from the continuous gridded profiles that linearly interpolates between sensors, we would implicitly assume that wave perturbations are vertically coherent between adjacent instruments regardless of the depth-separation. For an unchanging sensor geometry we would obtain self-consistent results, but the sensor geometry changes significantly between deployments. Inspecting the raw data shows that there is variance at all of the vertical scales that are resolved by the moorings.

The Gauss-Markov method explicitly gives one degree of freedom to each data point, and the magnitude of observational accuracy $\sigma$ defines how smooth the inversion will be between sensor depths. This method is a uniform way to treat all deployments regardless of sampling geometry. It also separates the question of what vertical scales can be resolved by the inversion into one of choosing $M$ that gives consistent results for all deployments.

The mode fits include a barotropic mode, which may at first appear inconsistent with our use of hydrographic data that cannot resolve barotropic motion. As previously described, however, the dynamic consistency between $p'_r$ and $\phi'$ requires that we make some choice of reference level, whether explicitly or implicitly. Though the exact choice will determine the absolute magnitude of the signal (Appendix A2), our interest in the baroclinic component is met by treating $\phi$ and $p'_r$ in the same fashion and not taking the magnitude at face value. All moorings exhibit barotropic amplitudes that are well correlated with those of the first baroclinic modes (BC1) and that are of similar magnitude. The correlation is strongest for the interior moorings ($R = 0.93$) and is weaker at the boundaries ($R = 0.57$ at WB2, $R = 0.76$ at WB3, $R = 0.83$ at EBH). This violates the assumption that modes are independent and the expectation that barotropic motion is significantly faster than baroclinic motion.

In practice, we found that including a barotropic mode in the mode inversion is necessary to maintain the choice of a zero reference level at the seafloor. Though this maintains consistency between $\phi$ and the mode reconstructions, we do not interpret the barotropic component of the fit. Since the barotropic mode is indeterminate and has an unknown relationship with the dynamical sense of the word, we refer to it as the depth-uniform response for the remainder of the article. Further discussion is given in Appendix A2.

The choices made for mode fitting depend strongly on the vertical resolution of the moorings. Our choice of $M < J$ was made for uniform results for all deployments. In contrast, Wunsch and Stammer (1997) chose to fit 5 modes to moorings with predominantly 3–5 current meters per mooring. Though no details were given on the sensitivity or robustness of his fits, he needed to consider significant correlation between mode amplitudes when quantifying the amount of variance recovered by subsets of modes. Similarly, our choice of excluding near-surface data was made because this region is inconsistently sampled and is highly sensitive for the inversion because all modes have strong signals at the surface. When high vertical resolution at the surface is not matched at depth, then the deep maxima that distinguish higher modes are not resolved properly. The inversion is then a balance between resolving high vertical structure in the surface layer (energy to higher modes) with smoothly fitting widely-spaced deep measurements (energy to lower modes). We have calculated mode decompositions that include the shallow sensors, and the results show only minor differences with those presented here. This is further proof that our method is robust.

In addition to numerical concerns, our choices reflect our interest in signals in the full water column. Surface signals are driven by very different dynamics that the harmonic motions described by vertical modes. Given that the moorings do not adequately monitor this layer, at best one microcat is in the bottom of the surface-mixed layer; uniform consideration of near-surface density anomalies is not tractable from our measurements.

# 5 Results

Having described the vertical mode decomposition, now we interpret how accurate it is and how well it can recover original measurements made by the moorings and independent measurements made by satellite altimetry.

## 5.1 Quantities and variables used for analysis

Three quantities are considered in the rest of this article: (1) the originally-measured and gridded signal following standard Rapid/MOCHA processing, (2) reconstructed signals from modal decompositions, and (3) SSH from altimetry. The original signal is broken into temporal perturbations as $\phi'$ or $p'_r$ and a time average $\langle \phi \rangle$. These quantities are calculated over each mooring deployment. The modal decomposition calculates mode amplitudes based on predefined mode shapes. Because the normalization of the mode shapes determines their relative magnitudes, it is necessary to multiply them together to obtain a physically meaningful result. This is done either at a specific vertical level (e.g. $F_n(z_0) P_n(t)$) or averaged over the water column using the vertical rms of the mode shape (namely $P_n(t) \int F_n^2 \, dz$). Reconstructions are formed by adding modes together, for which we can use all flat-bottomed (FB) modes ($M = 5$) or the first two modes, the depth-uniform mode and the first baroclinic mode (BC1). Reconstructions using the first two modes are based on decompositions with $M = 2$, and can be done either with flat-bottomed modes or with KB modes. As the constant of integration is undetermined for transport calculations based on vertical integrals of $p'_r$ or $\phi'$, we only consider time-perturbations assuming a reference level at the bottom.

SSH is used both for comparison to the surface pressure perturbation as well as for transport calculations. When calculating transports derived from SSH, we set $g\eta'$ as the amplitude of the first baroclinic mode (Wunsch and Stammer, 1997; Hirschi et al., 2009). The vertical structure comes from the flat-bottomed first baroclinic mode $F_1$, after which standard calculations with a bottom reference level yield time-fluctuations of transport.

All three of these quantities are expressed in the same units $m^2 s^{-2}$ by proper normalization (e.g. $\phi$, $p'_r$, and $g\eta$) and so their magnitudes can be directly compared. Though we do not present data from bottom pressure measurements, they need to be scaled by $\rho_o$ to obtain the same units.

## 5.2 Accuracy of mode decomposition

The mode decompositions are first quantified for their accuracy in recovering the original signal, which depends strongly on the number of modes used in the inversion.

By an "accurate" fit we mean one that meets the few expectations that we have in advance: the surface layer (above 140–200 m) should be coherent with the signals directly beneath it; and the reconstructions for each deployment should be comparable in variance and frequency content. The first criterion is easily broken if too many modes are solved for; even $M = 6$ is too large, which is caused by the Gauss-Markov method forcing the fit to zero in depth-ranges unconstrained by data. The second criterion relates to whether the changing vertical distribution of sensors between deployments is sufficient to change the statistics of the fit. This is to be avoided, otherwise the results would be biased by the instrument distribution.

As an example, detailed results are shown for WB5 (Fig. 3). The first deployment has no microcat at 250 m with adjacent microcats at 100 and 400 m (as seen by the median sensor depths shown in Fig. 3a). The reconstruction using all flat-bottomed modes ($M = 5$, Fig. 3b), however, gives surface results that are coherent with the signal at 400 m. There is a strong positive signal in the original data (Fig. 3a) at the end of 2004 measured by sensors at 50 and 100 m that is not recovered by the reconstruction. Such a signal was purposely excluded by limiting the inversion to data below 140 m, because the strong surface intensification implies a response forced by the atmosphere that does not contain energy throughout the water column. Generally, the $p'_r$ signals are strongest above the permanent thermocline (above 1000 m), which corresponds to the zero-crossing of the first baroclinic mode. Residuals of the full reconstruction (Fig. 3c) exhibit much lower vertical coherence than shown by the oceanic signal.

A quantitative assessment of the signal and the fits (Fig. 3d) show that the vertical rms of the original signal (black line) is $0.24 \pm 0.18 \, m^2 s^{-2}$ (average $\pm$ standard deviation), whereas that of the residuals with $M = 5$ (blue line) is two order of magnitude smaller ($0.008 \pm 0.004 \, m^2 s^{-2}$). The flat-bottomed and KB reconstructions (light blue and light green) with $M = 2$ have residuals an order of magnitude smaller than the signal (rms residuals of $0.03 \pm 0.03$ and $0.04 \pm 0.03 \, m^2 s^{-2}$), but give equivalent results. In a relative sense, the $M = 2$ reconstructions recover most of the large-amplitude signal, but when the signal is small they do not recover as large a percentage of the signal. Note that the rms operates on the 12–24 depths with direct measurements because errors are only defined at these depths.

The other stations (Fig. 4) have smaller amplitude fluctuations compared to WB5, but the fits are accurate to the same absolute accuracy. The stations near the boundary (WB2, WB3, EBH) have weaker oscillations that occur on faster time scales compared to the stations in the interior. The
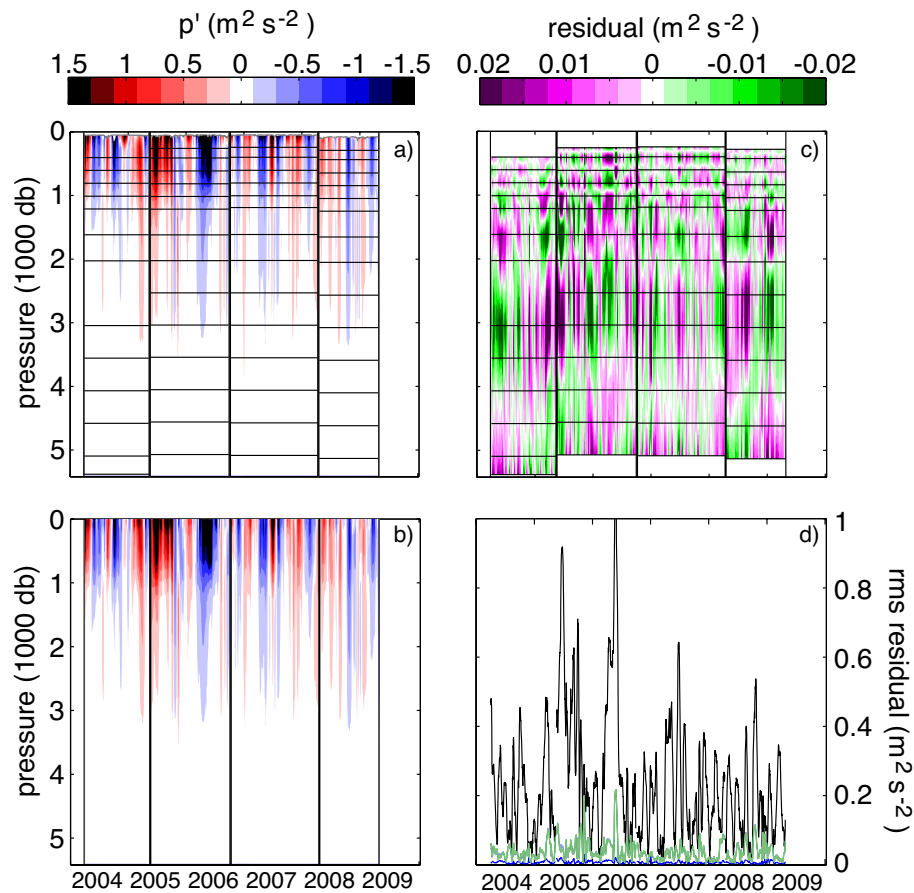
**Fig. 3.** An example reconstruction at WB5. **(a)** The original reduced pressure perturbation (in color), with median instrument depths (horizontal black lines) over each deployment. **(b)** The reconstructed reduced pressure perturbation using all 5 flat-bottomed modes. **(c)** The residual of the fits at constant depth levels over each deployment (note the enlarged color scale). **(d)** The vertical rms of the original signal (black), and the vertical rms residual of the reconstructed signal using all flat-bottomed modes (blue), using 2 flat-bottomed modes (light blue, obscured by green), and using 2 KB modes (green). Different deployment periods are delineated by vertical lines.

eastern stations (EB1 and EBH) lack strong near-surface fluctuations, in contrast to WB2 and WB3 that have signals intensified at the shallowest microcat. The surface-layer cut-off of 140 m for the WB moorings removes some of this near-surface signal, but often this signal extends beneath the surface-forced layer above 140 m. Data gaps from missing near-surface instruments strongly affect the reconstruction in the near-surface layer.

The rms deviations at each station (third column of Fig. 4) shows how well the signal in the vertical can be recovered by our mode decomposition at each time step. At all stations the decomposition effectively recovers large-amplitude events, but is less accurate during periods of weak signals. The frequency observed in the direct measurements increases noticeably from WB5 to WB2, and it is also high at EBH. With higher frequency fluctuations, these stations also have weak signals more frequently than in the center of the ocean.

The rms deviations can be summarized by calculating their time-averages to capture the dominant variance at each sta-

tion (Fig. 5a). The averaged deviation of the original signal varies from $0.16\ \mathrm{m^2\,s^{-2}}$ at WB2, up to $0.24\ \mathrm{m^2\,s^{-2}}$ at WB5, and down to $0.08\ \mathrm{m^2\,s^{-2}}$ at EBH. The rms deviations using all 5 flat-bottomed modes are factors of 10–30 smaller than the original signal ($0.019\ \mathrm{m^2\,s^{-2}}$ at WB2, $0.007\ \mathrm{m^2\,s^{-2}}$ at WB5, $0.006\ \mathrm{m^2\,s^{-2}}$ at EBH), while rms deviations using just the first two modes are factors of 3–6 smaller than the original signal ($0.05\ \mathrm{m^2\,s^{-2}}$ at WB2, $0.04\ \mathrm{m^2\,s^{-2}}$ at WB5, and $0.03\ \mathrm{m^2\,s^{-2}}$ at EBH).

From the original and error signals, we can calculate a variance explained by analogy to $R^2$ using $1 - (\text{rms dev}/\text{original rms})^2$ (Fig. 5b). Using this metric, the full mode reconstruction recovers more than 98 km of the variance at all stations. The $M = 2$ reconstructions still recover most of the variance, with values from 88 km at WB2 to 97 km at WB5. The $M = 2$ reconstructions give similar results regardless of whether the flat-bottomed or the KB modes are used, aside from at EBH where the $M = 2$
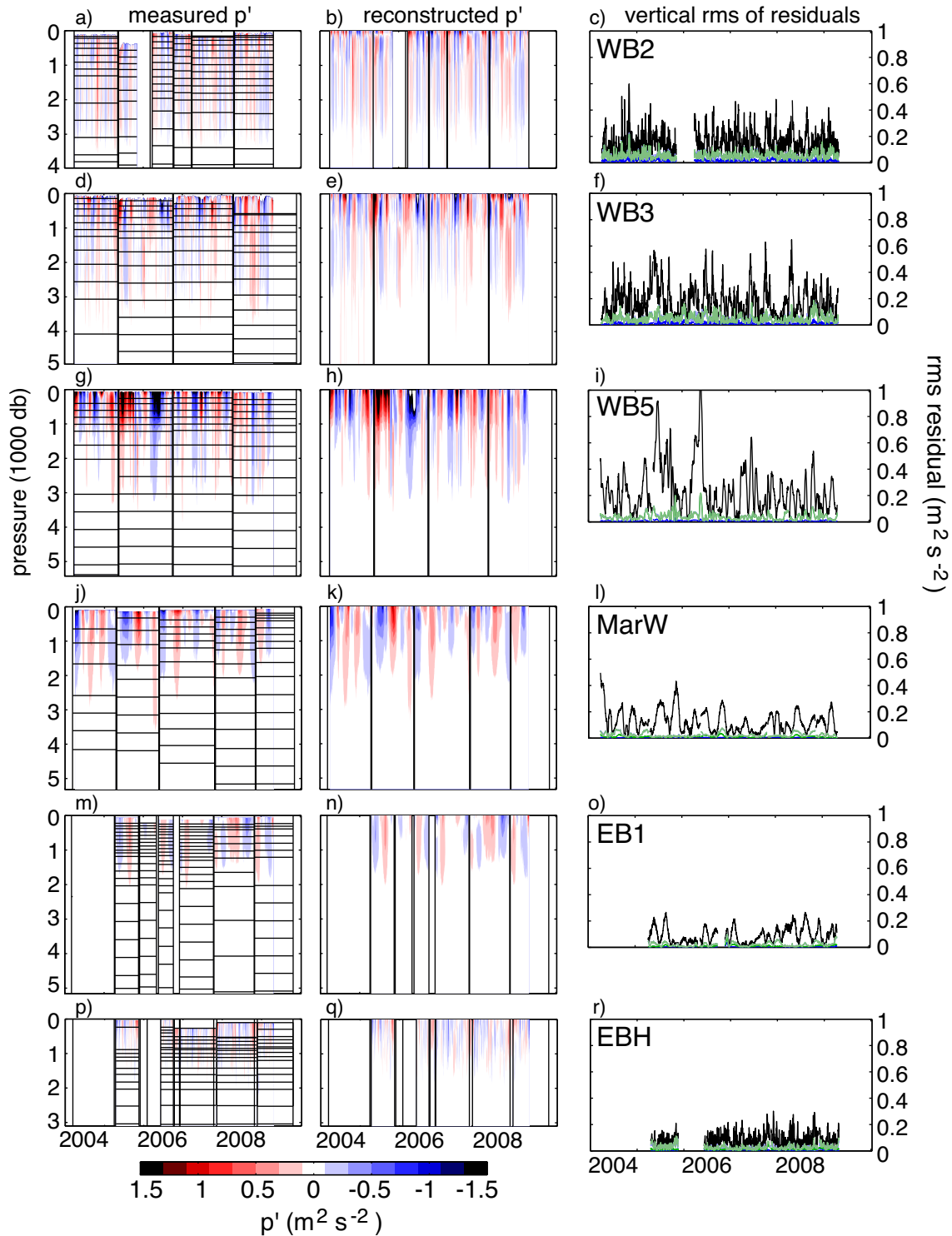
**Fig. 4.** Reconstructions for all moorings. (left column) The original $p'$ reduced pressure perturbation (in color), with median instrument depths (horizontal black lines) over each deployment. (center column) The reconstructed $p'$ using all 5 flat-bottomed modes. (right column) The vertical rms of the original signal (black), and the vertical rms residual of the reconstructed signal using all flat-bottomed modes (blue), using $M = 2$ flat-bottomed modes (light blue, obscured by green line), and using $M = 2$ KB modes (green). The rows from top to bottom are for moorings WB2, WB3, WB5, MarWest, EB1, and EBH. Each mooring deployment is delineated with vertical black lines.
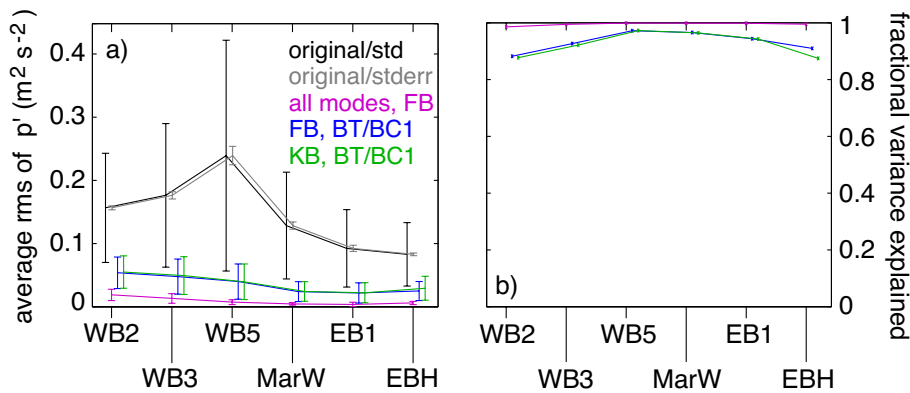
**Fig. 5.** (a) Time averages of vertical rms for the original signal (black with error bars), the residual from the complete flat-bottomed reconstruction (pink with error bars), the $M = 2$ flat-bottomed reconstruction residual (blue with error bars), and the $M = 2$ KB reconstruction residual (green with error bars). Standard deviations are shown over the entire record length with the error bars. In addition, the standard error of the mean for the original signal is also indicated (gray error bars). (b) Fractional variance (see text) explained by the full flat-bottomed reconstruction (purple), the $M = 2$ flat-bottomed reconstruction (blue), and the $M = 2$ KB reconstruction (green).

flat-bottomed reconstruction is slightly better (by 4 %) than the KB reconstruction.

The above results confirm that all the reconstructions account for the majority of the signal. This means that only the lowest few vertical modes (between 2 and 5) are efficient basis functions for explaining vertical structure at our mooring sites. Use of more modes than necessary would mix oceanographic signals with results dependent on alignment between the vertical sampling and the choice of modes.

Though time-series of the mode amplitudes are not shown, they are important indicators of whether the fitting method gives consistent results independent of the particular deployment. The choice of $M = 5$ does gives consistent results, but even increasing $M$ by 1–3 is sufficient for the sensor geometry to influence the mode decompositions.

### 5.3 Interpretation of vertical and modal structure

With the modal decomposition verified for consistency and accuracy, we can now interpret waves perturbations in mode space in addition to depth-space (Fig. 6). A depth-space interpretation is given first for reference. Note that the bottom referencing forces the deepest value to zero at all times.

At WB5, the standard deviation of $p'_r$ increases linearly above the base of the thermocline (at 1300 m) and is relatively uniform below. Approaching the western boundary three changes occur: the base of the thermocline or the zero-crossing of the first baroclinic mode rises 200 m, the surface intensification of $p'_r$ decreases, and the signal strength below the thermocline increases. To the east of WB5, the zero-crossing of the first baroclinic mode deepens further (Fig. 2). MarWest, EB1, and EBH also show a reduced surface intensification compared to WB5, but the signal strength below the thermocline remains weak.

In terms of mode-space, the surface-intensified signal at WB5 corresponds to a large and dominant contribution from BC1. The higher modes contribute little, and the depth-uniform mode reflects issues related to the bottom referencing, which are not of primary interest here. The change in vertical structure from WB5 to WB2 is also reflected in mode-space: the standard deviation of the BC1 decreases while those of higher modes increase, such that at WB2, BC1 is no longer dominant in the variance it describes. Similar though less strong changes occur from WB5 to the eastern boundary: the BC1 decreases in strength, but the higher modes remain weak. For comparing the flat-bottomed and the KB modes, it is necessary to do decompositions with the same number of each modes. The reason is clear (Fig. 6), in that the same total variance is spread between a fewer number of modes. Though the $M = 2$ reconstructions tend to have slightly larger amplitudes, they are consistent with each other and display similar trends across the basin.

The Gauss-Markov inversion gives error bounds for the mode amplitudes, the average value of which is shown by the dashed lines in Fig. 6a. For the full $M = 5$ reconstruction with the flat-bottomed modes, the average error given by the Gauss-Markov inversion is well below the rms amplitude of the modes. The weak amplitudes found for BC3 and BC4 at MarWest, EB1, and EBH are close to but above the average error. When fewer modes are inverted for, as for the KB $M = 2$ decomposition, the errors are even lower than those shown for the flat-bottom mode inversion with $M = 5$. Standard deviations of $M = 2$ reconstructions are shown in Fig. 6a for comparison with the observations (in black). Both the flat-bottom (blue) and KB (green) reconstructions capture the dominant vertical structure, with discrepancies above 200 m (indicated by a horizontal dashed line) because this region is excluded from the inversion, and at the bottom
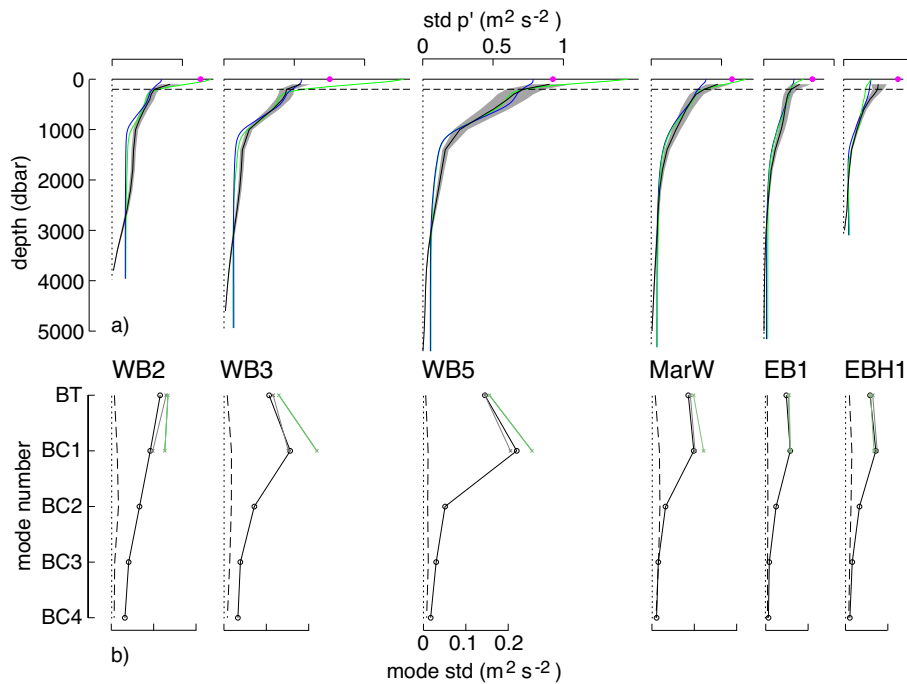
**Fig. 6. (a)** The standard deviation (std) of $p'$ against depth, for the direct observations (black) and 95 % confidence limits calculated with the F-statistic (gray), the flat-bottom $M = 2$ reconstruction (blue), the KB $M = 2$ reconstruction (green), and SSH (pink). **(b)** Standard deviation against mode number of $P_n$ multiplied by the vertical rms of $F_n$, for the complete $M = 5$ flat-bottomed modes (black), the flat-bottom $M = 2$ modes (gray), and the KB $M = 2$ modes (green). The dashed black line is the average error from the Gauss-Markov inversion for the complete $M = 5$ flat-bottom decomposition. The moorings are offset arbitrarily and are ordered from west to east.

because additional modes contribute to the zero variance implied by our choice of a bottom reference level.

The decrease in surface intensification is consistent with a decrease of SSH, as previously identified by Kanzow et al. (2009). Most directly, the reduction of SSH is related to a decrease in surface intensification above 1000 m, whether in a proportional or absolute sense. In mode space, however, it is only the BC1 mode that decreases from WB5 to WB2. As shall be shown later, this fact has a significant implication for the utility of SSH near the boundary.

At MarWest there is a slight mismatch between the BC1 mode and the observed vertical structure, but it does not affect the decomposition. The zero crossing of the flat-bottomed and KB BC1 modes are 200 m higher than indicated by the change in slope of the standard deviation of $p'$. At the other stations these two depths agree much better. The disagreement at MarWest cannot be remedied by considering KB modes with different propagation directions, such as might be expected for planetary waves deflected along $f/H$ contours as they cross the mid-Atlantic Ridge. If too many modes are fit, such a mismatch of modes and vertical structure could create depth-localized residuals in phase with the BC1 amplitude, which in turn yields undesired correlation between the modes. Though this effect is strong when $M = 8$, the use here of $M = 5$ greatly minimized it. If a large number of modes are used to extract oceanographic signals

(e.g. Lee et al., 2006), then care must be used to interpret the mode amplitudes.

## 5.4 Local near-surface signals

The first verification of the reconstruction is of the surface or near-surface signal, which allows comparison to be made with SSH. To avoid incorrectly ascribing modal dynamics to surface atmosphere-driven processes, we choose the 200 m depth level for making comparisons, similar to Kanzow et al. (2010) and consistent with excluding near-surface measurements from the fitting procedure.

The altimetric and mooring measurements are not expected to be exactly the same because of sampling and processing differences. SSH comes from a 7-day optimally-interpolated AVISO product that filters out variance at small spatial scales and short temporal periods. Altimetric returns are also contaminated close to coastlines. In contrast, the shallowest instrument on a mooring does not resolve the upper 60–120 m of the water column, has no horizontal smoothing, and is 2-day low-pass filtered. Differences between SSH and the mooring measurements will be incongruent because SSH includes surface-layer processes, whereas the mooring measurements do not. From visual inspection, surface processes are shallower on the western side of the transect than on the eastern side.
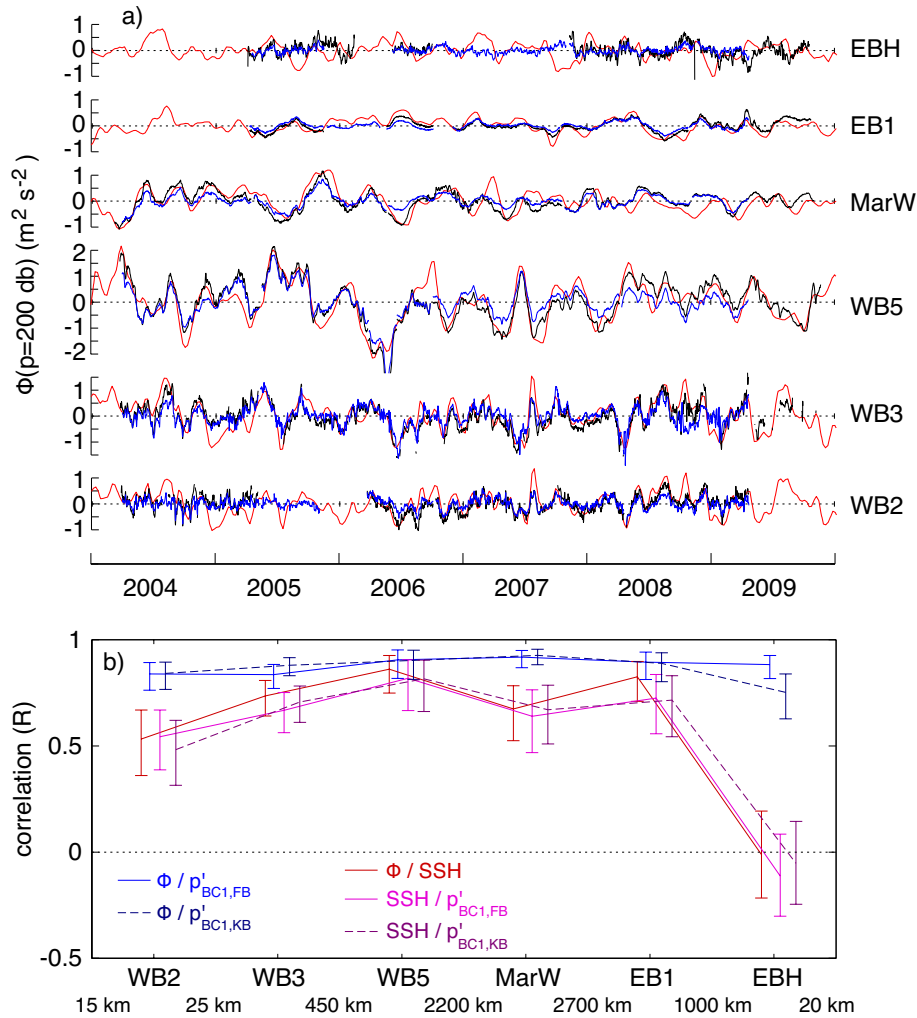
**Fig. 7.** Geopotential anomaly at 200 db. **(a)** Time series of geopotential anomaly for the original measurement ($\Phi$, black), the amplitude of the flat-bottomed BC1 mode at 200 db ($p'_{BC1} = P_1 F_1 (p = 200)$, blue), and SSH ($g\eta$, red). Stations are listed from the western boundary at the bottom to the eastern boundary at the top. **(b)** Correlations ($R$) between quantities shown earlier: $\Phi$ and $p'_{BC1,FB}$ (solid blue), $\Phi$ and $p'_{BC1,KB}$ (dashed blue), $\Phi$ and SSH (red), SSH and $p'_{BC1,FB}$ (pink), and SSH and $p'_{BC1,KB}$ (purple). Prior to calculating the correlations, $\Phi$, $p'_{BC1,FB}$, and $p'_{BC1,KB}$ are 10-day low-pass filtered. Error bars are calculated with a Fischer z-transform, and the degrees of freedom is the length of the time-series divided by the integral time-scale. Distances between the stations and to the coastlines are shown at the bottom.

Agreement between the directly-observed dynamic height, the BC1 reconstruction, and SSH is quite good (Fig. 7). The same pattern as previously noted holds for this comparison: the signals are strongest and agree most closely in the center of the basin, while the correlation is reduced at WB2 and at EB1. Reconstructions using $M = 2$ are as well correlated with SSH or the original signal as are the BC1 reconstructions shown. Including the depth-uniform mode, which is highly correlated with the BC1 mode, increases the magnitude of the reconstruction such that it matches the observed signal better.

Especially noticeable with this time series is that the signals at WB2 and EBH are high-frequency and lack the low-frequency fluctuations that dominate at WB5. The signal at

WB3 is intermediate in both magnitude and frequency content compared to WB5 and WB2. The pattern is different in the eastern basin, however: The amplitude decreases from WB5 to MarWest to EB1, but the dominant periods remain relatively long. The signal at the eastern boundary (EBH) is of similar magnitude to that at EB1 but has much more variance at high frequencies. As there are no full-depth moorings east of EB1, it is not possible to isolate how close to the boundary this change occurs (Chidichimo et al., 2010).

The time series (Fig. 7a) are quantified by calculating correlation coefficients ($R$) between the three variables (Fig. 7b). The $\phi'$ and $p'_r$ signals, though shown in Fig. 7a at full temporal resolution, are 10-day low-pass filtered prior to correlating with SSH so that all signals have the same

high-frequency cut-off. The error bars are 95 % confidence intervals calculated using a chi-square distribution for the Fischer z-transformed correlation coefficients. The degrees of freedom are calculated using the duration of the time series divided by the integral time-scale $\Gamma$, namely $\mathrm{DOF} = N \Delta t / \Gamma$ (Emery and Thomson, 1997). From west to east, the integral time-scales for $\phi'(p = 200\,\mathrm{db})$ are 17 d at WB2, 14 d at WB3, 53 d at WB5, 28 d at MarWest, 28 d at EB1, and 12 d at EBH. The addition of the depth-uniform component or the remaining BC modes does not significantly change the correlations.

The BC1 decomposition recovers the original signal well at 200 db (black, blue, and dark blue lines), with $R > 0.85$ at most stations but down to 0.75–0.80 at EB1 and EBH. The correlation of the original signal with SSH (red line) is maximum at WB5, is decreased by half at WB2, and is zero at EBH. The BC1/SSH correlation has similar structure across the basin compared to the original/SSH correlation. Despite this, the BC1/SSH correlation is slightly weaker compared to the original/SSH correlation. Small vertical scale features, which are not resolved by BC1 (presumably) contribute to the slightly better correlation between original/SSH.

The fact that MarWest has smaller correlation than the two stations on either side can be attributed to the slight mismatch of BC1 to the observations. Though this mismatch did not play a significant role when considering the residuals, it is more important when considering specific depth levels.

In contrast to the other stations, SSH is practically uncorrelated at EBH to subsurface signals. The surface intensification at EBH is very weak and is limited to above 200 db, and there is only a modest signal in the thermocline (200 to 1500 db).

One may also expect that bottom pressure might be correlated with the depth-uniform mode or the dynamic height signal, with or without subtracting the SSH signal. Though these correlations (not shown) are small and insignificant at WB5 and stations to the east, they are marginally significant at WB2 and WB3. The magnitudes ($R = 0.34 \pm 0.19$ explaining 10 km of the variance) are small enough that little utility is gained from them. The limited significance at WB2 does substantiate the findings of Bryden et al. (2009) that bottom pressure at WB2 is coherent with changes in baroclinic transport.

## 5.5 Local Transport signals

Since the Rapid/MOCHA array is intended to measure transport, we extend the previous section to vertically-integrated geopotential anomaly:

$$T^{\mathrm{local}} = \frac{1}{f} \int\limits_{-H}^{200\mathrm{m}} \phi' \, \mathrm{d}z. \tag{17}$$

Though geostrophic transports are calculated as the vertical integral of horizontal gradients of geopotential ($T =$ $(1/f) \int (\phi_{\mathrm{B}} - \phi_{\mathrm{A}}) \, \mathrm{d}z$), the equation above represents the amount of transport fluctuations implied by a single mooring. This approach is similar to that used by Kanzow et al. (2010) and Chidichimo et al. (2010) to isolate the influence of moorings at the western or eastern boundaries on the basin-wide geostrophic calculations, for which they used a time-averaged profile of $\phi$ to remove the influence of one boundary. The transport calculated is the total baroclinic signal from the seafloor to 200 m (see Appendix A2).

The three quantities discussed in the previous section are used here: the original geopotential anomaly $\phi'$, the BC1 reconstruction $p'_r$, and a reconstruction based on SSH. SSH fluctuations at a mooring location, after scaling by gravity, are taken as the amplitude of the BC1 mode. The surface expression is extrapolated into the water column using the vertical structure of BC1. The BC1 and SSH reconstructions are substituted into Eq. (17) to obtain a local transport perturbation.

Previously noted points are again apparent from Fig. 8, proceeding eastward from the western boundary: weak high-frequency signals near WB2, large low-frequency signals at WB5, weaker and longer-period signals at EB1, and weak high-frequency signals at EBH. The BC1 reconstructions accurately recover how standard deviations vary across the basin. Though the reconstruction standard deviations are always less than the original signal, the two boundary moorings (WB2 and EBH) exhibit the largest under-estimation. These two moorings exhibit different signals from the other moorings, so this is not surprising. Any decomposition will spread variance between all available modes, and so one might expect that only fitting two modes ($M = 2$) would allow the BC1 component to recover a greater variance. Half of the moorings (WB3, WB5, EB1) contradict this expectation, while the half that meets it only have minor increases of variance ($< 15\,\%$) that do not close the gap between the reconstruction and the original signal. For the interior moorings, the 20 km lower amplitude of the reconstructions suggests that higher modes are responsible for this fraction of the signal. For the two boundary moorings, correlations suggest that transport fluctuations do occupy the full water column and can partially be recovered from BC1 modes. At EBH the large correlation ($R = 0.8$, Fig. 8c) between the reconstruction and the original signal is in contrast to BC1 recovering a small fraction of the variance (10 %, Fig. 8b).

SSH signals accurately recover long-period fluctuations at WB3, WB5, and MarWest in terms of phasing, but the amplitude of SSH-derived transports is 30 km larger than the actual signals. This likely relates to the moorings not sampling the near-surface part of the water column. At WB2 and EBH, SSH slightly underestimates the transport signal by 20 %. SSH is more coherent at EBH with the integrated transport than with $\phi'$ at 200 db. Despite this, SSH at EBH poorly reflects the transport signal because SSH has a larger amplitude and is dominated by low-frequency motions.
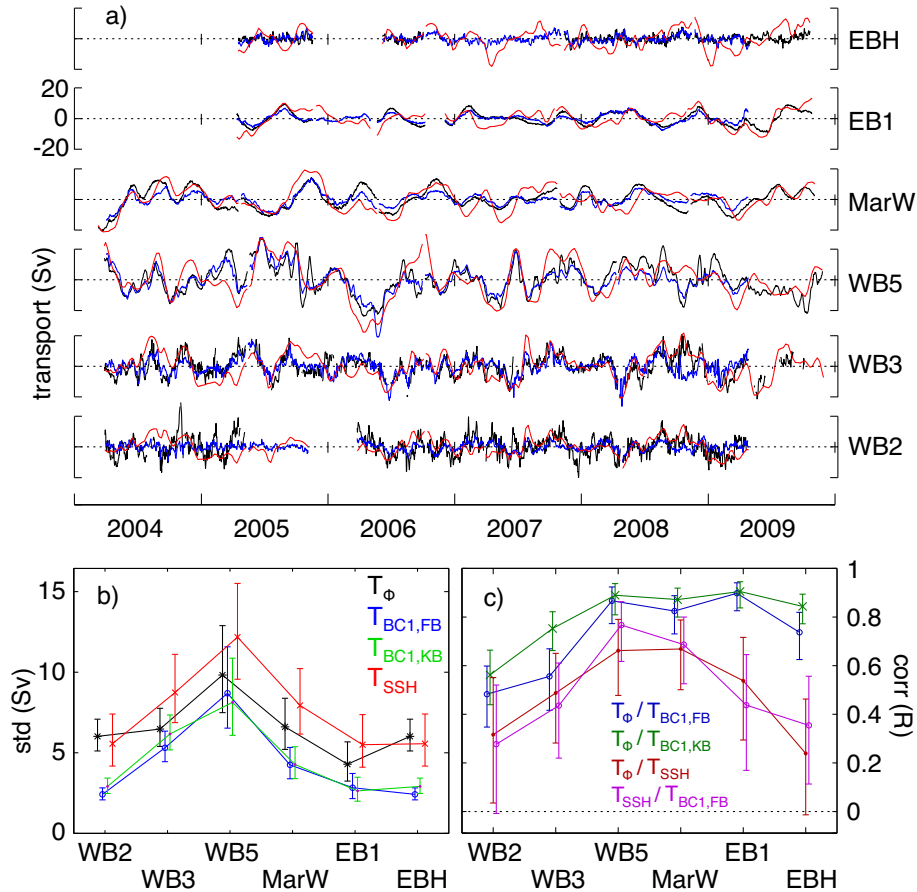
**Fig. 8.** Local transport calculations. **(a)** Time series of local transport for the original geopotential anomaly ($T_\Phi$, black), the flat-bottomed BC1-reconstructed mode fit ($T_{BC1,FB}$, blue), and the SSH-reconstructed signal ($T_{SSH}$, red). Stations are listed from the western boundary at the bottom to the eastern boundary at the top. **(b)** Standard deviation of $T_\Phi$ (black), $T_{BC1,FB}$ (blue), $T_{SSH}$ (red), and transport from the KB BC1-reconstruction $T_{BC1,KB}$ (green). **(c)** Correlations ($R$) between quantities shown earlier: $T_\Phi$ and $T_{BC1,FB}$ (blue), $T_\Phi$ and $T_{BC1,KB}$ (green), $T_\Phi$ and $T_{SSH}$ (red), and $T_{SSH}$ and $T_{BC1,FB}$ (purple). Prior to calculating the correlations, $T_\Phi$, $T_{BC1,FB}$, and $T_{BC1,KB}$ are 10-day low-pass filtered. Error bars are calculated with F-statistics for standard deviations and with Fischer z-transforms for correlations, and the degrees of freedom is the length of the time-series divided by the integral time-scale. Correlations between $T_{BC1,FB}$ and $T_{BC1,KB}$ are higher than 0.93 at all stations.

Correlations between transports calculated from original measurements, BC1 reconstructions, and SSH reconstructions (Fig. 8c) have smoother transitions across the basin than for $\Phi'$ at 200 db. BC1 reconstructions are significantly better than SSH at recovering the original transport signal. The variance recovered ($R^2$) varies from 22 km at WB2 to 76 km at WB5 to 56 km at EBH, and is smaller than for the rms residuals described by Figure 5. SSH has weak but similar correlations with the original signal or with the BC1 reconstructions, with a maximum of 40 km coherent variance at WB5 and MarWest and a minimum of less than 10 km at either boundary. BC1 reconstructions have similar correlations against SSH as does the original signal.

Most importantly for reconstructing basin-wide transport, SSH does not recover more than 10 km of the local transport variance at the two boundary stations compared to either the

original signal or the BC1 reconstruction. This low correlation occurs within one Rossby Radius of the boundary, which is 45 km at this latitude for BC1. If the eastern and western boundaries have uncorrelated fluctuations, as all evidence so far indicates, then the total explained variance from SSH will be no larger than 10 km ($R^2 = 0.06$). The BC1 reconstruction recovers more of the signal with $R^2 = 0.38$, but even this is not very accurate compared to the moorings. Note that this calculation is not directly comparable to the full basin-wide density gradients reported by Cunningham et al. (2007) because we do not extend the WB2 and EBH profiles with instruments and moorings at deeper depths.

## 5.6 Application to EBH

Having shown how the modal decomposition changes across 26.5° N, now we turn to a closer investigation of the EBH
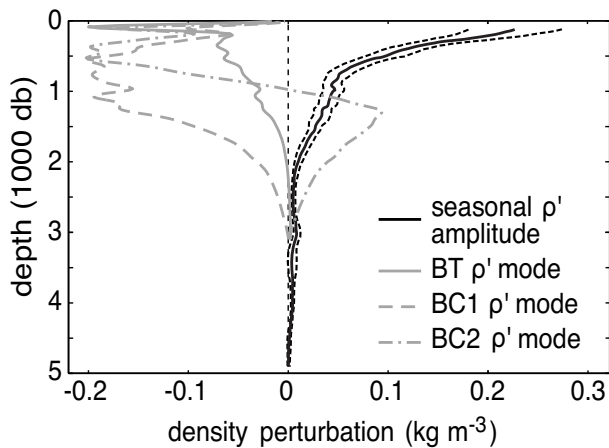
**Fig. 9.** Vertical modes and seasonal density anomalies at EBH. The profile of peak to peak seasonal density perturbation (solid black), with standard deviations (dotted black) and as calculated for the full EBH profile that extends out to EB1 at a water depth of $H = 5050$. Flat-bottomed density modes are shown for the barotropic (BT, solid gray), the first baroclinic (BC1, dashed gray), and second baroclinic modes (BC2, dash-dotted gray) calculated at EBH for which $H = 3000$ m (see text). All modes are normalized to have a minimum amplitude of –0.2 for visualization purposes and are of arbitrary sign.

mooring. Chidichimo et al. (2010) found that the seasonal cycle of density anomaly at EBH extends down to 1400 m, has a maximum in April–May and a minimum in October-November, and follows an annual cycle in wind stress curl by a quarter period. One interpretation of the seasonal cycle in density has been in terms of surface forcing of vertical modes (Kanzow et al., 2010), and so our framework allows a more detailed examination of the vertical structure of the seasonal cycle.

The first comparison to make is whether the shape of the seasonal density anomalies is similar to that expected for vertical modes. Unlike Kanzow et al. (2010), who used stratification at 60° W, we used stratification directly at EBH. The zero-crossing of the first baroclinic mode is 130 m shallower with EBH stratification compared to MarWest stratification, and is 400 m shallower than using MarWest stratification with a synthetic depth of 5000 m. For direct comparison to the observations, we first derive vertical modes for density.

Density modes $H_n$ can be calculated from pressure perturbations modes by applying the hydrostatic relation, or alternatively from vertical velocity modes via $H_n = N^2 G_n$. We derive that density modes are orthogonal with respect to $N^{-2}$.

The observed seasonal density perturbation (Fig. 9) decreases strongly from the surface to 800 m, decreases linearly from 800 m to 2000 m, and is close to zero below 2000 m. The signal is within a month of being in phase at all depths, though there is a hint from Chidichimo et al. (2010) that the

maximum signal at depths of 1000–1400 m leads that above 500 m by one month. This apparent phase lag could also be explained by vertical merging of moorings at different horizontal locations. None of the 3 lowest density modes is a clear fit to the observed vertical shape. Modes higher than the second baroclinic mode do not give a near-uniform phase throughout the water column. The first baroclinic mode has a uniform maximum from 400–1200 m and vanishes at the surface, which strongly contradicts the shape of the observed seasonal anomaly. The barotropic mode is the closest fit, although it misses the observed intensification between 200–800 m. Though a shape can be calculated for the barotropic density mode, it is much smaller in magnitude than the baroclinic signals. It is highly doubtful that the barotropic mode can be excited strongly for such long periods or that it is physically meaningful in general or on a sloping boundary. Since no single density mode is sufficient to describe the observations, we conclude that many modes must combine to give the observed profile. Correlations between the baroclinic modes are not large enough to indicate a dominant vertical structure at EBH.

Previously presented results on the accuracy of the mode reconstructions give further insight into how well the signal at EBH can be recovered with a modal analysis. Reconstructions with $M = 2$ and $M = 5$ do significantly better at recovering transport variance at EB1 (80 km for $M = 2$) compared to EBH (56 km for $M = 2$) (from Fig. 8). The reduced accuracy of low order vertical modes at EBH compared to EB1, despite the strong seasonal signal at EBH, contradicts the dominance of low order vertical modes at EBH suggested by Kanzow et al. (2010).

## 6 Discussion

The dataset provided by Rapid/MOCHA is well suited for studying large-scale planetary waves. The decent vertical resolution throughout the entire water column and the long time-series are essential for evaluating low-frequency motion, and the hydrographic measurements of density are particularly appropriate given how potential energy is dominant for large-scale planetary waves.

The main result from our analysis has been seen repeatedly in the results presented. Subsurface fluctuations in the center of the basin are large, are well described by a first baroclinic mode, and have long periods. These signals are accurately described by SSH, especially the large signals in the western basin. At the boundaries, however, the signals are weak, are poorly described by the first baroclinic mode, and have large variance at relatively short periods. These differences explain why SSH is of limited utility at the boundaries.

Though these results may appear obvious in hindsight, the agreement between SSH and vertical modes has often been assumed but has rarely been analyzed in detail. The decrease of the surface signal towards the western boundary has been

the focus of much recent attention (Wunsch, 2008; Kanzow et al., 2009; Zhai et al., 2010), but the underlying assumption has always been that it is solely the surface amplitude that is of importance. Similarly, studies that interpret SSH in terms of the first baroclinic mode assume that this relationship is stable and uniform at all horizontal locations, whether based on numerical modeling (Hirschi et al., 2007, 2009) or on ARGO observations (Willis, 2010). We have shown that this is a false assumption close to the boundaries at 26° N. Exactly where and how these assumptions fail gives useful insight into the local dynamical processes.

In particular, our finding of reduced agreement between BC1 motions and SSH or transport at the boundaries is concomitant with a change in the frequency content of the signals. This change is expected from theoretical considerations: time-scales in the interior are governed by slow geostrophic adjustment, whereas time-scales close to boundaries can be much faster because motions can be balanced against topographic gradients or through frictional effects. Many varieties of boundary waves (Kelvin waves, topographic Rossby waves, or mixed boundary waves) are possible, and frictional effects act as sources or sinks of potential vorticity.

Previous studies have considered similar issues in numerical models (Hirschi et al., 2007, 2009). Despite Hirschi et al. (2009) processing the numerical results in a fashion similar to how observations would be processed, the numerical data is entirely self consistent and "perfectly" sampled without measurement noise or noise from unrelated processes (e.g. tides), so it gives an upper limit for correlations between SSH and geopotential anomaly. The mooring measurements require substantial data processing, while the gridded SSH product requires even more, and so it was not known in advance how self-consistent the two independent datasets would be. Both studies show weak but marginally significant correlations on the boundaries at 26° N. Although our analyses are not directly comparable, we find larger correlations in the interior than suggested by their model. Our finding that the first baroclinic mode does not dominate at either the eastern or western boundary explains why even small errors in reconstructing boundary profiles can have large relative impacts on the resulting overturning calculation.

EOFs efficiently extract the dominant variability, but can give misleading results if the spectrum is continuous or if two modes are of equal amplitude (Wunsch, 1997). The results then are difficult to interpret dynamically. We also note that profiles of unit transport, calculated as the horizontal difference of geopotential anomaly between EBH and WB2, cannot be meaningfully interpreted as vertical modes. Vertical modes describe vertical oscillations at one horizontal location, and, even if two locations have the same stratification, using a single mode to explain the difference of two widely-separated profiles of geopotential anomaly is dynamically inappropriate and complicates interpretation. For this reason it is also necessary to consider the amplitude in addi-

tion to correlation, because subtracting two large signals that have small but incoherent errors will accentuate the errors, as is the case for basin-wide transport calculations. Our decomposition approach is in contrast to a statistical approach such as an empirical orthogonal function (EOF) analysis. A dynamical framework behind the vertical shapes allows theory to be applied to and tested against the observations. This feature will be exploited in future research.

We have found the simple flat-bottomed theory to be the most useful for interpretation despite its limitations. Once additional considerations are added to the flat-bottomed motionless-ocean modes, however, there is not a consensus on boundary conditions (Killworth and Blundell, 2003; Tailleux and McWilliams, 2001), how to incorporate forcing (Killworth and Blundell, 2007; Lapeyre, 2009), or what conditions invalidate the WKBJ approximation in the real ocean. In part, this is because varied observations highlight different components of the complete and continuous spectra of wave processes in the ocean. A comparison of vertical structures calculated from four theoretical assumptions (Hunt et al., 2012) did not find any theory to be adequate in describing velocities taken from a numerical model. We specifically investigated the more complete theory of Killworth and Blundell (2003). A critical but unavoidable side effect of increased complexity is that only a limited number of modes can be calculated. Regardless of the mode shapes, decompositions will find larger amplitudes when only two modes are resolved (depth-uniform and BC1) than when many more are. When the decomposition is only done for two modes (the depth-uniform and BC1 modes) with the flat-bottomed and the KB modes, comparable results in terms of magnitude and correlation are obtained. The flat-bottomed and KB modes have the greatest differences close to the sea surface, which itself is a region we seek to downweight in our analysis.

There are two ways to interpret our modal analysis: as picking out discrete wave signals (e.g. for the BC1 component), or as defining a spectrum (Nash et al., 2006). The discrete approach was favored here, as it lends itself to comparison with SSH and to transport-related questions raised by the purpose of the Rapid/MOCHA array. Despite having more than 12 instruments in the vertical, we find that only a limited number of modes (5) can be inverted for if the results are to be independent of the exact vertical placement of instruments within the typical mooring geometry used for the project.

The details of agreement between subsurface fluctuations, baroclinic modes, and sea surface height indicates the importance of near-surface signals and forcing. A clear example of the different conclusions reachable is a comparison of Chelton et al. (1998), Chelton et al. (2007), and Lapeyre (2009), in which altimetric SSH signals are interpreted respectively as non-linear Rossby waves, as oceanic eddies, or as forced surface-intensified waves. Different resolution SSH products and a different treatment of surface signals and forcing led to mutually exclusive conclusions. Similarly, studies based on

current meters (Wunsch, 1997) will respond preferentially to signals with strong kinetic energy at the depths sampled.

We minimized the influence of near-surface signals on our mode decompositions by excluding measurements shallower than 140 m or 200 m (depending on the station). There are many energetic surface processes, but not all of these processes are related to vertical modes. Some, such as surface buoyancy forcing or Ekman convergence, can be generation mechanisms for internal waves. A clear understanding of what spatial and horizontal time-scales are necessary to generate low-frequency planetary waves is complex and poorly understood (Killworth and Blundell, 2007), and we do not tackle it here. Forced planetary waves would further need to propagate downward over some horizontal distance before they feel the bottom (Johnson, 2011), before which point vertical modes would not be efficient basis functions.

Though one might hope that the different observing systems of subsurface dynamic height and SSH would be consistent measurements, this holds true often than desired, especially close to the boundaries. A third independent measurement that could be compared against its bottom pressure, which is also measured by Rapid/MOCHA. The frequency content of bottom pressure (Bryden et al., 2009) is much different from the moored hydrographic measurements, with large variance at high frequencies. We have attempted to find correlations between various combinations of geopotential anomaly, SSH, and bottom pressure, but practically no coherence has been found other than small correlation at WB2. Bottom pressure at WB2 has been investigated by Bryden et al. (2009), and, after removing many sources of noise, there is a signal coherent with local changes in geopotential anomaly.

We expect the Rapid/MOCHA measurements and the results of our vertical mode analysis to be similar in general to other subtropical regions. Equatorial and subpolar regions have different balances, set by changing contributions from baroclinic Rossby wave speeds, stratification effects (baroclinic around the equator and barotropic towards the poles), and topographic steering through $f/H$ contours.

The vertical structure of the seasonal density anomaly at EBH has interesting implications for the ultimate cause of this seasonal cycle. Our conclusion that multiple vertical modes are necessary to reproduce the vertical profile at EBH contradicts the conclusion of Kanzow et al. (2010) that the seasonal cycle is predominantly caused by the lowest two baroclinic modes. The fact that deep density anomalies slightly lead shallower density anomalies implies upward phase propagation and downward energy propagation, and is consistent with the fact that multiple modes are necessary to describe vertically propagating signals.

The hypothesis of low-order westward-propagating modes describing the seasonal cycle at EBH has two other limitations, one observational and one theoretical. As Kanzow et al. (2010) acknowledge, their model of wind-forced low-order baroclinic modes only allows for monotonic west-

ward propagation of vertical modes. No westward propagating signals, however, have yet been identified between EBH and EB1. Previous results found no seasonal cycle at EB1 (Chidichimo, 2010) and no significant correlations at any lag between EBH and EB1 for 50-day low-pass filtered overturning stream functions (Chidichimo et al., 2010). There is reduced transport variability at EB1 compared to EBH, seen by Chidichimo et al. (2010) and in our results (Fig. 8), which relates to different variances at periods shorter than 50 days (Chidichimo et al., 2010). Although we find similar variance in the lowest few modes at EBH and EB1, the reduced accuracy of mode decompositions (whether with $M = 2$ or $M = 5$) at EBH compared to EB1 further substantiates that the variability at each station is fundamentally different and could not be described by westward propagating signals. A breakdown of coherent westward transport is easier to believe for signals with energy at multiple modes, compared to signals with energy at low baroclinic modes.

A second limitation is that the close proximity of the continental slope will interfere with a flat-bottomed modal response. With the EBH moorings located close to the bottom at multiple horizontal locations along the slope, it is unknown whether the unsampled water column above the shallowest sensor on EBH1 (for instance) would exhibit the same seasonal cycle as that measured at the same depth by moorings further east. Near-coastal wind reversals typically lead to seasonal upwelling and downwelling that rely on proximity to the boundary. The presence of a quarter-period phase lag between wind stress curl and the seasonal cycle (Chidichimo et al., 2010) is consistent with damped forcing by wind. The hint of upward phase propagation with a month-long phase delay compared to the 12-month long cycle suggests that the ocean response to wind-forcing is faster than the seasonal cycle of the wind forcing. Even if the apparent phase delay arises from vertical merging of moorings at different horizontal locations, the oceanic response still appears to occur much faster than the seasonal cycle in wind. The high mode-number content and lack of westward propagation further support the seasonal signal being a damped and forced response instead of a freely propagating feature.

An alternative explanation, consistent with the seasonal signal being confined to EBH, is a forced response that has a vertical structure that decays exponentially from the surface (Killworth and Blundell, 2007). Regardless of the type of vertical structure, theoretical explanations of trapping to the boundary will require consideration of bottom topography.

The expected process can also be motivated by the constraint on horizontal scales given by topography and wind-forcing. The Rapid/MOCHA moorings are located in a broad canyon between the Canary Islands and the North African coast that is 100 km wide at the location of EBH1 and narrows towards the African coast. If there is upwelling induced circulation, the topographic ridge of the Canary Island chain will prevent a meridionally-uniform response as

typically found in well-known eastern boundary upwelling regions. The zonal scale is indicated by that of wind stress, which appears to be less than 100 km at 16°W (Kanzow et al., 2010). Location is also important: significant seasonal density signals are measured at EBH3 and to the east, which corresponds to longitudes east of 14°W. The wind-stress curl used by Kanzow et al. (2010) to explain the seasonal cycle is taken at 26.5° N, 16.1°W. Chidichimo et al. (2010) extracted wind-stress curl further east (at 27.12° N, 15.38°W), a location half-way between EBH1 and EBH2 where the zonal scale of wind-stress curl is 40 km (Chidichimo, 2010).

At EBH there can be two responses to divergence-free wind stress. Ignoring boundaries and friction, Ekman pumping will depress the base of the mixed layer, and the vertical displacement vanishes at the seafloor and is close to zero at the surface (K. Shimizu, personal communication, 2011). The vertical shape of this response is similar to the shape of the barotropic mode for isopycnal displacement, the only difference being in the thin mixed layer, but can be reconstituted by a linear composition of many baroclinic modes. A similar response happens adjacent to boundaries when Ekman transport is perpendicular to the boundary: the base of the mixed layer is displaced vertically, with displacements going to zero at the surface and at the seafloor along the slope. The difference for coastal upwelling, however, is that displacements decay away from the coastline. This forcing mechanism would require no additional complexities to explain why the seasonal signal vanishes between EBH and EB1.

These hypotheses about the cause of seasonal signal at EBH would ultimately need to be substantiated by observations about the spatial extent of the seasonal signal at the eastern boundary (M. P. Chidichimo, 2012).

## 7   Conclusions

Although fitting vertical modes is a well known procedure, its application to moored hydrographic data is not straightforward and we present a technique to do so. Our method is designed to extract signals that span the water column in a uniform manner for all mooring deployments, and yields robust results with small residuals.

By comparing the observations, the modal decompositions, and sea surface height across the Atlantic at 26° N, we find that:

– subsurface fluctuations in the center of the basin are large, are well described by a first baroclinic mode, have long periods, and are accurately described by SSH.

– at the boundaries, subsurface signals are weak, are less well described by the first baroclinic mode, have large variance at short periods, and are poorly described by SSH. These changes occur within one Rossby radius (45 km) of the western boundary, and along the slope of the eastern boundary.

– comparison of the annual cycle of density at EBH to vertical modes shows that the vertical structure requires a linear combination of many baroclinic modes. This is supported by the decomposition at EBH, with the two lowest modes not being as successful as at other stations in recovering geopotential anomaly or transport signals.

These findings are a clear explanation for why mid-ocean waves or eddies do not strongly influence the methodology of using end-point density profiles to obtain basin-wide geostrophic transport at 26° N: not only do BC1 amplitudes decrease at the boundaries, but they also represent less of the total variance. Because the boundaries clearly enable other motions than the eddies or waves seen in the interior, wave-boundary interactions will be essential for interpreting geostrophic transports calculated by the Rapid/MOCHA array.

## Appendix A

Though typically used to describe internal waves, reduced pressure perturbation is also dynamically equivalent to geopotential anomaly. This similarity leads to consideration of the depth-uniform component of fit, which, though interesting in its own right, is simply removed from our analysis by our choice of reference level and by including a depth-uniform mode in the mode decomposition

## A1   Equivalence of geopotential anomaly and reduced pressure perturbation

Geopotential anomaly $\phi$ is defined as

$$\phi \equiv \int\limits_0^p \left( \frac{1}{\rho} - \frac{1}{\rho_{35,0,p}} \right) \mathrm{d}p,$$

where the integrand is specific volume anomaly. A Reynolds decomposition of density into $\rho = \langle \rho \rangle + \rho'$ (where, for the quantity $x(t)$, $x'(t)$ is a time-perturbation and $\langle x \rangle$ is a time-average) separates the time-average and time-varying (or perturbation) quantities. This decomposition is convenient because $1/\rho$ can be simplified with a Taylor expansion of the form $1/(1 + \rho'/\langle \rho \rangle) = 1 - \rho'/\langle \rho \rangle + \left( \rho'/\langle \rho \rangle \right)^2 - \cdots$ after application of the Boussinesq approximation $\rho'/\langle \rho \rangle \ll 1$. Keeping only the first term of this expansion, specific volume anomaly can be divided into constant and fluctuating components according to

$$\phi = \langle \phi \rangle + \phi' = \int\limits_0^p \left( \frac{1}{\langle \rho \rangle} \frac{1}{1 + \rho'/\langle \rho \rangle} - \frac{1}{\rho_{35,0,p}} \right) \mathrm{d}p$$

$$\approx \int\limits_0^z \left( \frac{1}{\langle \rho \rangle} - \frac{1}{\rho_{35,0,p}} - \frac{\rho'}{\langle \rho \rangle^2} \right) \mathrm{d}p.$$

Substituting, replacing $\mathrm{d}p$ according to the hydrostatic approximation, and applying the Boussinesq approximation again (namely that $\langle\rho\rangle(z) \sim \rho_0$),

$$\phi' = -\int_0^p \frac{\rho'}{\overline{\rho}^2}\,\mathrm{d}p = -\int_0^z \frac{\rho'}{\overline{\rho}^2}(-\rho g\,\mathrm{d}z) = -\frac{g}{\rho_0}\int_z^0 \rho'\,\mathrm{d}z$$

demonstrates that $\phi'$ is equivalent to $p_r'$ under the above approximations. Note that a time-constant geopotential anomaly profile $\langle\phi\rangle(z)$ is the only difference between the full geopotential anomaly $\phi$ and either perturbation quantity $p_r'$ or $\phi'$.

## A2 Depth-uniform component of pressure perturbation

Invoking a reference level is typically performed when calculating geostrophic transports from two profiles of $\phi$, either ad hoc (0 at the surface or the bottom) or referenced to a point or horizontally-averaged velocity measurements (Lherminier et al., 2007). The same referencing must be done for profiles of $\phi$ at a single horizontal location, as indicated by $C$ in Eq. (1).

The application of referencing for low-frequency motion is less obvious because velocities are related to differences between two stations, $\phi_A - \phi_B$, for which the reference velocity is related to $C_B - C_A$. Analyzing measurements at a single mooring, however, there is only a single profile and so there is no information about horizontal gradients.

Referencing a profile of $p'$ has been investigated in the context of internal waves at tidal velocities, although it is not typically compared to the more familiar question of reference level. Many investigators remove a depth-uniform component following Kunze et al. (2002)

$$\overline{p_r'} = \frac{g}{\rho_0 H}\int_{-H}^0 \int_z^0 \rho'(z)\,dz\,dz,$$

though this is strictly true only under a rigid lid assumption over a flat bottom. Physically, removing $\overline{p_r'}$ from $p_r'$ decouples barotropic motion from baroclinic motion and prevents generation of baroclinic waves by barotropic flow. While such an assumption is relatively easy to assess for tidally forced signals, by analyzing whether barotropic tides flow perpendicular to isobaths, such an assumption is not obvious in the open ocean where wind and buoyancy forcing are ubiquitous but sporadic and where barotropic waves propagate much faster than baroclinic waves.

Adjustments to the depth-uniform barotropic correction of Kunze et al. (2002) are necessary over sloping bathymetry, but neither Kelly et al. (2010) nor Gerkema (2011) found a consistent method to reference $p'$ and to separate barotropic and baroclinic motion. The corrections are small, are only noticeable at the surface and bottom, and depend on the surface displacement of the barotropic tide. Our interest in low frequency planetary waves, which are broad band and typically are not generated by barotropic motion, suggests that the influence of sloping bathymetry is smaller and less cleanly described by these results for tidal internal waves.

The research cited above on separating barotropic and baroclinic motions in $p'$ is also counter to previous assumptions made for our analysis. The WKBJ approximation that allows use of local vertical modes already neglects the importance of horizontal gradients. We expect that a continuous spectrum of horizontal wavelengths for planetary waves would complicate a quantitative evaluation of the WKBJ assumption. In any case, the relatively long wavelengths expected of planetary waves implies that a sloping boundary would likely be important only at the eastern boundary. That the EBH profile consists of short bottom moorings at multiple horizontal locations further complicates applying results from Kelly et al. (2010). The western boundary is steep enough to be considered a wall (for WB2), an entirely different problem from waves over sloping bathymetry, while moorings away from the interior are on relatively flat bottom topography.

Previous studies have indicated that, at the western boundary, a time-averaged level of no motion is found between the Antilles Current and the Deep Western Boundary Current at a depth of 1000 m (Johns et al., 2008). All moorings west of and including WB5 have no velocity measurements, so the time-averaged level of no motion is unknown. Applying such a time-averaged level of no motion to meridional velocities would result in all velocity perturbations at that depth being zero. This is a strong assumption that would bias our results, and further cannot be implemented because a level of no motion cannot be readily applied to a vertical profile of density measurements without horizontal information.

For lack of an alternative applicable at all stations, we chose a near-bottom reference level of 0 for the observations. Our decomposition shows strong correlations between amplitudes of the barotropic and BC1 modes, which contradicts the assumption that modes behave linearly and independently of each other. Though it is unavoidable to have a depth-averaged component in our mode fits in order to maintain consistency, we limit our analysis to time-fluctuations and to vertical shear and ignore the absolute transport. For the mode decompositions, the depth-uniform barotropic mode responds strongly to the near-bottom reference level. As this component of the fit would require a focused attempt to understand and is tangential to the analysis presented here, we simply include it for consistency but do not interpret it by itself.

# References

Alford, M. H.: Redistribution of energy available for ocean mixing by long-range propagation of internal waves, Nature, 423, 159–162, 2003.

Bryden, H. L., Mujahid, A., Cunningham, S. A., and Kanzow, T.: Adjustment of the basin-scale circulation at 26° N to variations in Gulf Stream, deep western boundary current and Ekman transports as observed by the Rapid array, Ocean Sci., 5, 421–433, doi:10.5194/os-5-421-2009, 2009.

Chelton, D. B., de Szoeke, R. A., Schlax, M. G., El Naggar, K., and Siwertz, N.: Geographic variability of the first baroclinic Rossby radius of deformation, J. Phys. Oceanogr., 28, 433–460, 1998.

Chelton, D. B., Schlax, M. G., Samelson, R. M., and de Szoeke, R. A.: Global observations of large oceanic eddies, Geophys. Res. Lett., 34, L15606, doi:10.1029/2007GL030812, 2007.

Chidichimo, M. P.: Eastern-boundary baroclinic variability and the meridional overturning circulation at 26.5 N, Reports on Earth System Science (Ph.D. thesis) 84, Max Planck Institute for Meteorology, Hamburg, Germany, iSSN 1614–1199, 2010.

Chidichimo, M. P., Kanzow, T., Cunningham, S. A., Johns, W. E., and Marotzke, J.: The contribution of eastern-boundary density variations to the Atlantic meridional overturning circulation at 26.5° N, Ocean Sci., 6, 475–490, doi:10.5194/os-6-475-2010, 2010.

Cunningham, S. A., Kanzow, T., Rayner, D., Baringer, M. O., Johns, W. E., Marotzke, J., Longworth, H. R., Grant, E. M., Hirschi, J. J.-M., Beal, L. M., Meinen, C. S., and Bryden, H. L.: Temporal variability of the Atlantic meridional overturning circulation at 26.5 degrees N, Science, 317, 935–938, doi:10.1126/science.1141304, 2007.

Emery, W. J. and Thomson, R. E.: Data analysis methods in physical oceanography, Pergamon, Elsevier Science Ltd, Oxford, UK, 1 Edn., 1997.

Gerkema, T.: Comment on "Internal-tide energy over topography" by S. M. Kelly et al., J. Geophys. Res., 116, C07029, doi:10.1029/2010JC006611, 2011.

Gill, A. E.: Atmosphere-Ocean Dynamics, vol. 30 of International Geophysics Series, Academic Press, San Diego, CA, 666 pp., 1982.

Hirschi, J. J.-M., Killworth, P. D., and Blundell, J. R.: Subannual, seasonal and interannual variability of the North Atlantic merid-ional overturning circulation, J. Phys. Oceanogr., 37, 1246–1265, 2007.

Hirschi, J. J. M., Killworth, P. D., Blundell, J. R., and Cromwell, D.: Sea Surface Height Signals as Indicators for Oceanic Meridional Mass Transports, J. Phys. Oceanogr., 39, 581–601, doi:10.1175/2008JPO3923.1, 2009.

Hunt, F. K., Tailleux, R., and Hirschi, J. J.-M.: The vertical structure of oceanic Rossby waves: a comparison of high-resolution model data to theoretical vertical structures, Ocean Sci., 8, 19–35, doi:10.5194/os-8-19-2012, 2012.

Johns, W., Kanzow, T., and Zantopp, R.: Estimating ocean transports with dynamic height moorings: An application in the Atlantic Deep Western Boundary Current at 26 degrees N, Deep-Sea Res. Pt. I, 52, 1542–1567, doi:10.1016/j.dsr.2005.02.002, 2005.

Johns, W. E., Beal, L. M., Baringer, M. O., Molina, J. R., Cunningham, S. A., Kanzow, T., and Rayner, D.: Variability of shallow and deep western boundary currents off the Bahamas during 2004-05: Results from the 26 degrees N RAPID-MOC array, J. Phys. Oceanogr., 38, 605–623, doi:10.1175/2007JPO3791.1, 2008.

Johnson, G. C.: Deep signatures of southern tropical Indian Ocean annual Rossby waves, J. Phys. Oceanogr., in press, doi:10.1175/JPO-D-11-029.1, 2011.

Johnson, H. L. and Marshall, D. P.: A Theory for the Surface Alantic Response to Thermohaline Variability, J. Phys. Oceanogr., 32, 1121–1132, 2002.

Kanzow, T., Cunningham, S. A., Rayner, D., Hirschi, J. J.-M., Johns, W. E., Baringer, M. O., Bryden, H. L., Beal, L. M., Meinen, C. S., and Marotzke, J.: Observed flow compensation associated with the MOC at 26.5 degrees N in the Atlantic, Science, 317, 938–941, doi:10.1126/science.1141293, 2007.

Kanzow, T., Hirschi, J. J.-M., Meinen, C. S., Rayner, D., Cunningham, S. A., Marotzke, J., Johns, W. E., Bryden, H. L., Beal, L. M., and Baringer, M. O.: A prototype system of observing the Atlantic Meridional Overturning Circulation — scientific basis, measurement, and risk mitigation, J. Operational Ocean., 1, 19–28, 2008.

Kanzow, T., Johnson, H. L., Marshall, D. P., Cunningham, S. A., Hirschi, J. J.-M., Mujahid, A., Bryden, H. L., and Johns, W. E.: Basin-wide integrated volumne transports in an eddy-filled ocean, J. Phys. Oceanogr., 39, 3091–3110, doi:10.1175/2009JPO4185.1, 2009.

Kanzow, T., Cunningham, S. A., Johns, W. E., Hirschi, J. J.-M., Marotzke, J., Baringer, M. O., Meinen, C. S., Chidichimo, M. P., Atkinson, C., Beal, L. M., Bryden, H. L., and Collins, J.: On the seasonal variability of the Atlantic meridional overturning circulation at 26.5°N, J. Climate, 23, 5678–5698, doi:10.1175/2010JCLI3389.1, 2010.

Kelly, S. M., Nash, J. D., and Kunze, E.: Internal-tide energy over topography, J. Geophys. Res., 115, C06014, doi:10.1029/2009JC005618, 2010.

Killworth, P. and Blundell, J.: Long extratropical planetary wave propagation in the presence of slowly varying mean flow and bottom topography. Part I: The local problem, J. Phys. Oceanogr., 33, 784–801, 2003.

Killworth, P. D. and Blundell, J. R.: Planetary wave response to surface forcing and instability in the presence of mean flow and topography, J. Phys. Oceanogr., 37, 1297–1320,

doi:10.1175/JPO3055.1, 2007.

Killworth, P. D., Chelton, D. B., and de Szoeke, R. A.: The speed of observed and theoretical long extratropical planetary waves, J. Phys. Oceanogr., 27, 1946–1966, 1997.

Kunze, E., Rosenfeld, L. K., Carter, G. S., and Gregg, M. C.: Internal Waves in Monterey Submarine Canyon, J. Phys. Oceanogr., 32, 1890–1913, 2002.

Lapeyre, G.: What vertical mode does the altimeter reflect? On the decomposition in baroclinic modes and on a surface-trapped mode, J. Phys. Oceanogr., 39, 2857–2874, doi:10.1175/2009JPO3968.1, 2009.

Lee, C. M., Kunze, E., Sanford, T. B., Nash, J. D., Merrifield, M. A., and Holloway, P. E.: Internal tides and turbulence along the 3000-m isobath of the Hawaiian Ridge, J. Phys. Oceanogr., 36, 1148–1164, 2006.

Lherminier, P., Mercier, H., Gourcuff, C., Alvarez, M., Bacon, S., and Kermabon, C.: Transports across the 2002 Greenland-Portugal Ovide section and comparison with 1997, J. Geophys. Res., 112, C07003, doi:10.1029/2006JC003716, 2007.

MacKinnon, J. A. and Gregg, M. C.: Shear and Baroclinic Energy Flux on the Summer New England Shelf, J. Phys. Oceanogr., 33, 1462–1475, 2003.

Nash, J. D., Kunze, E., Lee, C. M., and Sanford, T. B.: Structure of the Baroclinic Tide Generated at Kaena Ridge, Hawaii, J. Phys. Oceanogr., 36, 1123–1135, 2006.

Tailleux, R. and McWilliams, J.: The effect of bottom pressure decoupling on the speed of extratropical, baroclinic Rossby waves, J. Phys. Oceanogr., 31, 1461–1476, doi:10.1175/1520-0485(2001)031¡1461:TEOBPD¿2.0.CO;2, 2001.

Watts, D. R. and Kontoyiannis, H.: Deep-ocean bottom pressure measurement - drift removal and performance, J. Atmos. Oceanic Technol., 7, 296–306, 1990.

Willis, J. K.: Can in situ floats and satellite altimeters detect long-term changes in Atlantic Ocean overturning?, Geophys. Res. Lett., 37, L06 602, doi:10.1029/2010GL042372, 2010.

Woodgate, R. A. and Killworth, P. D.: The problem of the barotropic mode in deriving pressure from density by using vertical normal modes, J. Geophys. Res., 101, 3765–3768, 1996.

Wunsch, C.: The Ocean Circulation Inverse Problem, Cambridge University Press, Cambridge, United Kingdom, 1996.

Wunsch, C.: The vertical partition of oceanic horizontal kinetic energy, J. Phys. Oceanogr., 27, 1770–1794, 1997.

Wunsch, C.: Mass and volume transport variability in an eddy-filled ocean, Nat. Geosci., 1, 165–168, 2008.

Wunsch, C. and Stammer, D.: Atmospheric Loading and the Oceanic "Inverted Barometer" Effect, Rev. Geophys., 35, 79–107, 1997.

Zhai, X., Johnson, H. L., and Marshall, D. P.: Significant sink of ocean eddy energy near western boundaries, Nat. Geosci., 3, 608–612, doi:10.1038/NGEO943, 2010.